Cavin1 intrinsically disordered domains are essential for fuzzy electrostatic interactions and caveola formation

Vikas A. Tillu[1], James Rae[1,2], Gao Ya[1], Nicholas Ariotti[3,4], Matthias Floetenmeyer[2], Oleksiy Kovtun[1,5], Kerrie-Ann McMahon[1], Natasha Chaudhary[1,6], Robert G. Parton[1,2]* and Brett M. Collins[1]*

1. The University of Queensland, Institute for Molecular Bioscience, St. Lucia, Queensland, 4072, Australia.
2. Centre for Microscopy and Microanalysis, St. Lucia, Queensland, 4072, Australia.
3. Electron Microscope Unit, The University of New South Wales, Kensington, New South Wales, Australia.
4. Department of Pathology, School of Medical Sciences, The University of New South Wales Kensington, New South Wales, Australia.
5. Current address: MRC Laboratory of Molecular Biology, Cambridge Biomedical Campus, Cambridge, UK.
6. Current address: The Lunenfeld-Tanenbaum Research Institute, Mount Sinai Hospital, Toronto, Canada.

Running Title: Cavin1 disordered sequences in caveola formation

*Corresponding authors: Robert Parton, Ph: +61 (0)7 33462032, Email: r.parton@imb.uq.edu.au
Brett Collins, +61 (0)7 33462043, Email: b.collins@imb.uq.edu.au

Keywords – caveolae, Cavin, coiled-coil, intrinsically disordered protein, MURC, phase separation, PTRF, SDPR, SRBC, undecad repeat

Summary (150 words)

Caveolae are spherical-shaped nanodomains of the plasma membrane, generated by cooperative assembly of caveolin and cavin proteins. Cavins are cytosolic peripheral membrane proteins with negatively charged intrinsically disordered regions (DR1-3) that flank positively charged α-helical regions (HR1 and HR2). Here we show that the three DR domains of Cavin1 are essential for caveola formation and dynamic trafficking of caveolae. Electrostatic interactions between DR and HR regions promote liquid-liquid phase separation behaviour of Cavin1, assembly of Cavin1 oligomers in solution, generation of membrane curvature, association with caveolin-1 (CAV1), and Cavin1 recruitment to caveolae in cells. Removal of the first disordered region causes irreversible gel formation *in vitro* and results in aberrant caveola trafficking through the endosomal system. We propose a model for caveola assembly whereby fuzzy electrostatic interactions between Cavin1 and CAV1 proteins, combined with membrane lipid interactions, are required to generate membrane curvature and a metastable caveola coat.

52 **Introduction**

53 Caveolae ('*little caves*') are membrane invaginations with a diameter of 50-60 nm that are abundant
54 in the plasma membrane of many cell types such as muscle fibres, endothelial cells and adipocytes.
55 These membrane nanodomains are important for an array of different functions including
56 endocytosis, intracellular signalling, lipid and fatty acid homeostasis and response to membrane stress
57 [1-3].

58 Although the precise details of caveola biogenesis remain enigmatic their assembly requires
59 the activities of two families of proteins - caveolins and cavins - and their coordinated interactions
60 with membrane lipids and cholesterol. The integral membrane proteins of the caveolin family (CAV1,
61 CAV2 and muscle specific CAV3) are synthesized at the endoplasmic reticulum and trafficked via
62 the Golgi apparatus to the plasma membrane [4]. Caveolins have an unusual hairpin structure that
63 inserts into the membrane bilayer, with an extended N-terminal domain and α-helical C-terminal
64 domain exposed to the cytoplasm [3, 5, 6]. When expressed on its own in mammalian cells the core
65 caveolin CAV1 is diffusely localised in the plasma membrane and is unable to form spherical
66 caveolae in the absence of cavins [4, 7]. However, CAV1 is able to generate membrane vesicles similar
67 to caveolae (h-caveolae) upon heterologous expression in *Escherichia coli* [8]. This points to an
68 intrinsic capacity of CAV1 to generate membrane curvature, which is thought to be enabled by the
69 specific lipid composition of *E. coli* membranes. In metazoan cells however, the additional presence
70 of the peripheral membrane cavin proteins is required for the formation of native caveolae. In
71 particular, Cavin1 and CAV1 are together required and sufficient to generate a minimal core system
72 for caveola formation at the plasma membrane. Other cavin family members require Cavin1 for their
73 recruitment and are thought to provide regulatory or tissue-specific activities [7, 9, 10].

74 All cavin proteins share a highly characteristic domain architecture consisting of two core α-
75 helical regions (HR1 and HR2) with relatively high sequence conservation [11, 12]. These are connected
76 by three intrinsically disordered regions (DR1, DR2 and DR3), that possess very little sequence
77 homology but share the property of being enriched in negatively-charged residues (**Fig. 1A**). Cavin
78 proteins can assemble into homo- and hetero-oligomeric complexes that form a protein coat on the
79 cytosolic face of caveolae; and the essential isoform Cavin1 can form homo-oligomers that drive
80 caveola formation in the absence of other family members [11, 13, 14]. The N-terminal α-helical HR1
81 domain of Cavin1 forms a core trimeric coiled-coil structure that also promotes heteromeric
82 interactions between other members of the Cavin family [11]. A surface exposed patch of basic amino
83 acid residues in the HR1 domain has affinity for phosphoinositide lipid headgroups including
84 phosphatidylinositol-4,5-bisphosphate (PI(4,5)P_2) [11]. The C-terminal α-helical HR2 region of Cavin1
85 is unique in the cavin family as it also contains a stretch of repeated undecad sequences (11-mers)
86 predicted to form a second coiled-coil structure termed UC1 (undecad of Cavin1) [10]. Basic amino

acids within the HR2 and UC1 domains can associate with phosphatidylserine (PS) to regulate caveola formation and stability [10]. These two α-helical lipid interacting sites are important for membrane recruitment and for generating caveolar membrane curvature. However, the molecular mechanisms of caveolar membrane association and higher-order assembly of cavins with caveolins at the cell surface are largely unknown.

In this study we examined the role of the uncharacterised DR domains of Cavin1 in caveola formation. The DR domains of Cavin1 are strictly required for caveola assembly, and a systematic dissection of these intrinsically disordered regions showed that there are minimal acidic sequences within the DR domains that are essential for caveolar targeting, *in vitro* membrane remodelling and homo-oligomeric Cavin1 complex assembly. We find that Cavin1 undergoes electrostatically-driven self-association via its disordered regions that promotes liquid-liquid phase separation (LLPS) *in vitro*, that it can co-phase separate with CAV1, and this is dependent on specific sequence properties of the two proteins. Perturbing the DR domain-mediated dynamics of Cavin1 self-association has profound effects on Cavin1 and CAV1 localisation and caveolar trafficking in cells. Our results lead us to propose a model for caveola assembly involving 'fuzzy' electrostatic interactions by Cavin1 at the CAV1/membrane interface to generate a metastable caveola coat.

Results

Cavin1 forms electrostatically-driven oligomers that depend on DR1 and DR3 domains

The cavin family proteins all share distinguishing structural similarities with each other, consisting of disordered N- and C-terminal domains DR1 and DR3, a central disordered region DR2, and interspersed α-helical coiled-coil region HR1 and predicted α-helical region HR2 (**Fig. 1A**). The trimeric coiled-coil HR1 domain and C-terminal HR2 domains are both rich in basic amino acid residues, while the three DR domains instead possess a high proportion of acidic amino acid residues. This alternating electrostatic charge distribution is a distinctive and conserved feature of all family members (**Fig. S1A**), indicating it is an essential characteristic of the proteins. We also used the D2P2 web server [15] to analyse the sequence of Cavin1 for predicted regions of disorder, and confirmed that the DR1, DR2 and DR3 regions are predicted to be intrinsically disordered as suggested by previous secondary structure analyses [10, 11] (**Fig. S1B**). Interestingly, sites of phosphorylation in Cavin1 are predominantly found in the DR1, DR2 and DR3 domains, while sites of ubiquitylation are concentrated in the HR1 and HR2 regions. In subsequent experiments the boundaries of the mouse Cavin1 domains are defined as: DR1 (1-44), HR1 (45-155), DR2 (156-209), HR2 (210-310), and DR3 (311-392) (**Fig. 1A**). Expression constructs used in this study are outlined in **Fig. S2.**

We recently proposed that the predominantly negatively charged DR sequences of Cavin1 may associate with the positively charged HR domains to promote intra and/or inter molecular electrostatic interactions required for coat assembly [12]. To probe the role of electrostatic interactions, we used fluorescence correlation spectroscopy (FCS) to measure the diffusional properties of purified GFP-tagged Cavin1 in both 500 mM NaCl (high salt) and 150 mM NaCl (iso-osmotic salt concentration). According to polymer theory, the diffusivity of protein molecules in solution decreases with increasing intermolecular interactions due to molecular crowding limiting its molecular motion [16]. GFP-Cavin1 (100 nM concentration) showed a remarkable decrease in its diffusivity with the reduction of ionic strength from 500 mM NaCl (12.01 ± 3.03 μm^2/sec) to 150 mM NaCl (4.02 ± 0.50 μm^2/sec) **(Fig. 1B)**. This indicates that at physiological salt concentrations Cavin1 can form homomeric oligomers with an average hydrodynamic radius ~55 nm, similar to those observed previously [4, 14], and that this self-association is dependent on electrostatic interactions. In contrast to full-length Cavin1, removal of either N- or C-terminal DR1 or DR3 domains prevents this electrostatically driven self-assembly at lower physiological salt concentrations **(Fig. 1B)**.

Next, we sought to understand the role of DR sequences in oligomeric assembly of Cavin1 in a more representative cellular milieu. For these experiments we used MCF7 cells, which lack caveolae and do not express any caveolin or cavin proteins [14, 17, 18]. GFP-tagged Cavin1 proteins were transiently expressed and FCS analysis was used to measure the diffusivity of each protein in cell lysates (all at 150 mM NaCl). Full length GFP-Cavin1 in MCF7 cell lysates forms relatively

140 heterogenous large molecular weight species in solution with slow diffusive properties (6.35 ± 2.35
141 μm^2/sec) **(Fig. 1C)** similar to purified recombinant GFP-Cavin1. In contrast to purified recombinant
142 GFP-Cavin1-ΔDR1, the N-terminal DR1 deletion in cell lysates showed a similar (although tending
143 to faster) rate of diffusion to the full-length protein (7.65 ± 4.40 μm^2/sec) **(Fig. 1C)**. Complete
144 deletion of the C-terminal DR3 region of GFP-Cavin1-ΔDR3 however, significantly increased the
145 diffusivity of Cavin1 in MCF7 lysates (18.54 ± 6.22 μm^2/sec), similar to the recombinant GFP-
146 Cavin1-ΔDR3 **(Fig. 1C)**. Overall these studies demonstrate a role for the DR sequences in
147 electrostatically-driven oligomerisation of Cavin1 in solution.
148
149 **Cavin1 undergoes liquid-liquid phase separation (LLPS) influenced by the DR domains**
150 There is an increasing awareness of the role of intrinsically disordered sequences in generating
151 membraneless organelles via liquid-liquid phase separation (LLPS) or 'demixing' of proteins and
152 associated molecules in solution. Such demixing phenomena can be driven by a variety of
153 mechanisms, including cation-π and π-π stacking, interactions with polyanions such as RNA, and
154 intermolecular electrostatic interactions [19-22]. A number of recent studies have shown that membranes
155 can be platforms for nucleating and transporting phase-separated assemblies, or in turn be regulated
156 and organised via LLPS-mediated processes [23-34]. It has also been proposed that the formation of
157 phase-separated condensates can perform physical work on their surroundings, including at the
158 membrane-cytosol interface to generate membrane curvature [35-38]. Because of the demonstrated
159 importance of disordered regions in Cavin1 for its assembly behaviour, we decided to assess if
160 purified Cavin1 is able to form supramolecular assemblies leading to LLPS *in vitro*.
161 Purified recombinant GFP-Cavin1 expressed in *E. coli* remains dispersed in solution at both
162 iso-osmotic NaCl concentration (150 mM) and at high NaCl concentration (750 mM) within a protein
163 concentration range of 1 to 10 μM **(Fig. S3A)**. However, when Dextran T-500 (1.25% w/v) was added
164 as a macromolecular crowding agent [39, 40] full-length GFP-Cavin1 rapidly formed spherical liquid
165 droplets at 150 mM NaCl even at low protein concentrations (0.1 μM) **(Fig. S3B and Fig. S3C)**. This
166 is well below estimated cellular concentration of Cavin1 of 3 μM [41]. These droplets increased in size
167 with increasing protein concentration in the range 1 to 10 μM **(Fig. 2A)**. Increasing the salt
168 concentration strongly inhibited the ability of GFP-Cavin1 to undergo LLPS, consistent with a role
169 for electrostatic intermolecular interactions [20, 42]. We also tested both purified full-length Cavin1-GFP
170 expressed in mammalian HEK293 cells, and un-purified Cavin1-GFP in MCF7 cell lysates, and found
171 that both preparations underwent similar salt-sensitive LLPS (**Fig. S4A and S4B**). Lastly, we
172 assessed if Cavin1 could undergo LLPS in cells. When over-expressed in MCF7 cells, which lack
173 CAV1 and caveolae, we found that GFP-Cavin1 on its own remained diffuse and did not form
174 droplets. However, after testing several conditions we found that if cells were treated with cholesterol

following serum starvation GFP-Cavin1 rapidly formed cytoplasmic condensates as well as membrane-associated tubules (**Fig. S4C**). Similar results were observed in CAV1-/- mouse embryonic fibroblasts (MEFs) (**Fig. S4D**). We speculate this alters the equilibrium of Cavin1 interactions with phospholipid membranes, thus promoting self-association and LLPS behaviour.

Deletion of the C-terminal DR3 domain had a small but reproducible effect on the tendency of GFP-Cavin1-ΔDR3 to undergo LLPS, with droplet formation showing greater sensitivity to increasing ionic strength and protein concentration **(Fig. 2A; Fig. S3B and S3C)**. Deletion of the DR1 domain had a dramatic effect leading Cavin1 to transition into non-spherical coacervates at all protein and salt concentrations **(Fig. 2A; Fig. S3B and S3C)**. Fluorescence recovery after photobleaching (FRAP) was used to analyse the diffusion of proteins within the liquid droplets and the ability of GFP-Cavin1 to exchange with bulk solution. GFP-Cavin1 ($\tau_{1/2}$ ~20s) and GFP-Cavin1-ΔDR3 ($\tau_{1/2}$ ~10s) showed rapid fluorescence recovery after photobleaching, indicating there is ready exchange of protein molecules within the droplets as expected for liquid droplets **(Fig. 2B, 2C)**. GFP-Cavin1-ΔDR1, however, showed virtually no recovery **(Fig. 2B, 2C)**, suggesting that gel formation has occurred and the truncated protein is unable to diffuse within the condensates [19, 43]. Overall, these analyses highlight the importance of electrostatic interactions in promoting self-association and subsequent LLPS behaviour by Cavin1, and suggest distinct roles of DR1 and DR3 sequences in this process.

Cavin1 can promote co-phase separation with N-terminal regions of CAV1

Although Cavin1 and CAV1 are associated together in caveolae, it remains unclear whether they interact ~~directly~~ with each other via direct protein-protein interactions. CAV1 has a unique structural domain architecture shared with other caveolins, consisting of an N-terminal disordered sequence (1-60) followed by an oligomerization and scaffolding domain (61-100), intramembrane domain (101-133) and a C-terminal membrane associated α-helical domain (134-179) (**Fig. 3A**) [2, 5]. We hypothesized that the N-terminal disordered sequence of CAV1 may enable CAV1-cavin1 association through interactions involving liquid-liquid phase separation. To test this, we first purified full length CAV1 tagged with Maltose binding protein (MBP) and GFP-binding nanobody protein (GBP) [44] in non-ionic detergent n-dodecyl β-D-maltoside (DDM) (1.2 mM). MBP-GBP-CAV1 was labelled with GFP through high affinity binding to GBP for visualization, and unlabelled purified Cavin1 was used in a co-phase separation assay (**Fig. 3B and 3C**). Like GFP-Cavin1, unlabelled Cavin1 formed liquid droplets with addition of dextran T-500 (1.25% w/v) observed in bright field image as transparent liquid drops. In the absence of Cavin1 MBP-GBP-CAV1 did not undergo LLPS on its own **(Fig. 3B).** However, when GFP-labelled MBP-GBP-CAV1 was mixed with Cavin1 it was

209 recruited to Cavin1 liquid droplets **(Fig. 3C)**. Interestingly MBP-GBP-CAV1 appeared to form a shell
210 around the Cavin1 droplets rather than undergo complete co-mixing.

211 We next probed the mutual roles of Cavin1 and CAV1 disordered sequences in Cavin1-CAV1
212 co-phase separation. To this end we generated several mCherry-tagged truncation mutants in the
213 region CAV1 (1-100) encompassing the disordered N-terminus, oligomerization and scaffolding
214 domains **(Fig. 3A)**. Similar to previous reports we found that mCherry-CAV1(1-100) formed a higher
215 molecular weight oligomer by gel-filtration, while any truncations of this sequence resulted in
216 monomeric proteins **(Fig. S5A)** [13]. Like full-length MBP-GBP-CAV1, the mCherry-CAV1(1-100)
217 sequence was able to undergo LLPS with GFP-Cavin1 droplets, again forming an outer shell around
218 the core GFP-Cavin1 droplets (**Fig. 3D**). In contrast truncated mCherry-CAV1 constructs (1-30), (30-
219 80) and (1-80) were all unable to undergo co-phase separation with Cavin1. These results confirm
220 that the mCherry-CAV1(1-100) interaction with GFP-Cavin1 is specific, and we also observed
221 similar results using unlabelled Cavin1 (**Fig. S5B**). Interestingly, while mCherry-CAV1(1-100) was
222 also able to co-phase separate with the Cavin1 N-terminal deletion GFP-Cavin1-ΔDR1, it did not
223 associate with droplets formed by the C-terminal deletion of GFP-Cavin1-ΔDR3 **(Fig. 3D)** suggesting
224 that the Cavin1 DR3 sequences are essential for CAV1 – Cavin1 association.

225 To further pinpoint the molecular mechanism of CAV1 and Cavin1 co-phase separation, we
226 made three sets of mutations in CAV1 (1-100) (**Fig. 3A**). Two highly conserved segments ^{54}RDP^{56}
227 and ^{68}FEDVIAEP^{75} were mutated to alanine, or random glycine and serine (mutants M1 and M2
228 respectively). A third mutant M3 was constructed to replace all charged residues (Glu, Asp, Arg, Lys)
229 in the disordered region (1-80) with alanine. CAV1 mutants M1 and M2 both formed oligomers
230 similar to wild-type mCherry-CAV1(1-100) as assessed by their gel filtration profiles, whereas
231 mutant M3 surprisingly migrated as a monomer **(Fig. S5A)**. Mutants mCherry-CAV1(1-100) M1 and
232 M2 both underwent co-phase separation with GFP-Cavin1 similar to the wild-type CAV1(1-100),
233 while mutant M3 failed to associate with Cavin1 droplets **(Fig. 3D)**. These studies indicate that the
234 association between CAV1 and Cavin1 is driven at least in part by interactions involving liquid phase
235 condensation, with co-mixing driven by their respective disordered sequences.

236

237 **The Cavin1 DR sequences are essential for membrane remodelling *in vitro***

238 We previously showed that Cavin1 and Cavin2 possess an intrinsic ability to tubulate artificial lipid
239 membranes using negative stain electron microscopy [11]. To examine this membrane remodelling by
240 Cavin1 at higher resolution, we first performed cryoelectron microscopy (cryoEM) analysis of
241 samples after mixing purified Cavin1 with small unilamellar vesicles (SUVs) composed of Folch
242 lipid extracts. We observed formation of an extensive network of membrane tubules (34 ± 5 nm, 12
243 tubules, 2 independent experiments) possessing a Cavin1 protein coat using both negative stain

244 electron microscopy and cryoEM **(Fig. 4A)**. Although tubulation of Folch membranes was most
245 efficient, Cavin1 could also tubulate liposomes consisting of PC/PE/PI(4,5)P_2 (**Fig. S6A**). In addition,
246 Cavin1-GFP expressed and purified from HEK293 cells could also tubulate Folch membranes
247 similarly to the bacterially expressed protein **(Fig. S6B)**. Examination of the Cavin1-coated tubules
248 in three dimensions by cryoelectron tomography (cryoET) revealed a striated but relatively
249 heterogeneous pattern of protein densities around the tubules (**Fig. 4B; Movie S1**). These are similar
250 to structures previously observed on the cytosolic face of caveolae using fast-freeze deep-etch [45, 46]
251 and conventional EM methods [47-49], and with the elongated rod-like structures of isolated Cavin1
252 observed by negative staining EM [11]. These experiments indicate that Cavin1 possesses an inherent
253 membrane remodelling activity, driven by large scale oligomeric assembly on the membrane surface.
254 The importance of Cavin1 DR domains in self-association and LLPS next raised the question
255 as to whether they play a role in its key ability to physically remodel membranes. To this end, we
256 used the *in vitro* membrane remodelling assay to investigate their importance in generating membrane
257 curvature. We expressed and purified a range of Cavin1 DR domain truncations with an N-terminal
258 His-ubiquitin (HisUb) tag (**Fig. 4C; Fig. S2**) and used the membrane tubulation assay combined with
259 negative stain EM to analyse their ability to remodel mammalian (Folch) synthetic phospholipid
260 membranes (**Fig. 4D**). It was immediately apparent that complete removal of the N-terminal DR1 and
261 C-terminal DR3 domains abolished the ability of Cavin1 to tubulate liposomes *in vitro*. Shorter
262 truncations showed that while the N-terminal DR1 deletion Cavin1(10-392) still formed membrane
263 tubules, these were relatively infrequent and of a smaller diameter (~10 nm), whereas further deletion
264 of N-terminal DR1 sequences in Cavin1(30-392) prevented the formation of membrane tubules
265 altogether. The C-terminal DR3 deletion mutant Cavin1 (1-345) formed membrane tubules similar to
266 full length Cavin1. However, the deletion of further amino acids from the C-terminus in Cavin1(1-
267 330) completely inhibited membrane tubulation. For those DR truncation mutants that lacked
268 membrane remodelling activity we observed instead a propensity to cause liposome clustering. This
269 likely occurs because these Cavin1 constructs can now bind adjacent phospholipid vesicles via
270 multiple positively charged surfaces of the HR1 and HR2 domains, unrestrained by compensating
271 negatively-charged DR1 and DR2 sequences [11]. Overall, these studies define a core Cavin1 sequence
272 (10-345) required for Cavin1 to efficiently promote membrane curvature.
273 We next examined the ability over time of purified GFP-Cavin1 to modulate giant
274 multilamellar vesicles (GMVs) doped with 0.1 mol% fluorescent Bodipy-TMR PI(4,5)P_2 analogue.
275 GFP-Cavin1 showed strong localised clustering at the membrane surface compared to other
276 membrane remodelling proteins **(Fig. 5A)** [50, 51], and possessed a remarkable membrane sculpting
277 activity as indicated by the rapid collapse of GMVs over a period of several minutes **(Fig. 5B)**. We
278 performed similar experiments with Rhodamine B-PE as a fluorescent marker of GMVs and observed

279 similar protein clustering as well as membrane sculpting activity (**Fig. S6C**). In contrast, although
280 both the N- and C-terminal DR deletions of Cavin1 still bound efficiently to the GMVs, they did not
281 display any significant membrane sculpting activity **(Fig. 5C, 5D)**. With Cavin1-ΔDR1 we also often
282 observed a characteristic accumulation of the protein at the interface between adjoining vesicles
283 leading to the clustering of the GMVs **(Fig. 5E)**. Overall, these studies using GMVs and SUVs show
284 that while the DR1 and DR3 domains are dispensable for membrane binding, they have an essential
285 role in the ability of Cavin1 to sculpt the curvature of phospholipid membranes.
286
287 **Cavin1 disordered sequences are essential for interacting with CAV1 and forming caveolae**
288 Our studies *in vitro* highlight several properties of Cavin1 that are dependent on its disordered
289 sequences. Firstly, DR1 and DR3 of Cavin1 are important for the formation of a large scale associated
290 state and LLPS promoted by electrostatic interactions, and the DR1 domain is required for the
291 dynamic properties of Cavin1 in LLPS; removal of the DR1 domain results in gel formation and
292 prevents its free diffusion within the condensates. The Cavin1-ΔDR1 construct also displays a
293 capacity to bind and cluster membrane vesicles *in vitro*. Secondly, minimal sequences of Cavin1 DR1
294 and DR3 are required for membrane remodelling. Lastly, the C-terminal DR3 domain of Cavin1 is
295 required for the association with CAV1 in co-mixed liquid droplets *in vitro*. To examine the
296 importance of Cavin1 disordered N- and C-terminal domains to functional caveola formation, we
297 next analysed the localisation of the DR1 and DR3 truncation mutants in cells (**Fig. 6A**). The prostate
298 cancer PC3 cell line was used, which expresses CAV1 but does not express any members of the Cavin
299 family so that CAV1 is diffusely localised at the plasma membrane [7, 9] (**Fig. S7A**). Expression of full-
300 length GFP-Cavin1 in PC3 cells fully restores the formation of caveolae with CAV1 (in the absence
301 of other cavins), providing a functional readout for Cavin1 activity [7, 9, 10, 52]. Using either standard
302 confocal microscopy (**Fig. S7A)** or confocal fluorescence with Airyscan super-resolution imaging
303 (**Fig. 6A)**, full length GFP-Cavin1 showed a characteristic punctate distribution and co-localised with
304 CAV1 at the plasma membrane. In contrast, after removal of the C-terminal domain GFP-Cavin1-
305 ΔDR3 is unable to promote caveola formation, does not co-localise with CAV1, and now accumulates
306 in the cytosol and also associates extensively with microtubules **(Fig. 6A, Fig. S7B)**. This is
307 consistent with a previous report of a similar C-terminal truncated Cavin1 (residues 1-322) in CHO
308 cells [53]. FRAP analysis of GFP-Cavin1-ΔDR3 on microtubules showed a fast fluorescence recovery,
309 indicating a dynamic exchange with the cytoplasm or diffusion along the microtubules (**Fig 6B,**
310 **Movie S2**). Interestingly, when microtubules were depolymerised with nocodazole this resulted in
311 redistribution and condensation of GFP-Cavin1-ΔDR3 to form spherical droplets in the cytosol (**Fig.**
312 **6C; Fig. S7B; Movie S3**). These also showed fast exchange of protein molecules with the bulk
313 cytoplasm suggestive of liquid-droplet behaviour. This suggests a dynamic equilibrium exists

between cytosolic, liquid droplet and microtubule associated states of the GFP-Cavin1-ΔDR3 truncation.

Strikingly, expression of GFP-Cavin1-ΔDR1 resulted in the formation of large intracellular structures that also contained endogenous CAV1 **(Fig. 6A; Fig. S7A)**. A C-terminal tagged Cavin1-ΔDR1-GFP construct showed similar clusters co-localised with CAV1, confirming this phenotype is not influenced by the location of the GFP tag (**Fig. S7C**). To analyse these structures in more detail, we performed co-localisation experiments of GFP-Cavin1-ΔDR1 with various cellular markers. While no overlap was seen with the Golgi complex, lysosomal or recycling endosomal membrane markers, a significant proportion of GFP-Cavin1-ΔDR1 and endogenous CAV1 were found to colocalise with the early endosomal marker EEA1 (**Fig. S8A)**. Airyscan microscopy revealed that clusters of EEA1 positive endosomes surrounded the GFP-Cavin1-ΔDR1 and CAV1 positive structures (**Fig. 6D; Fig. S8B**). We then performed transferrin uptake assays in PC3 cells expressing either mCherry-Cavin1 or mCherry-Cavin1-ΔDR1 using transferrin labelled with Alex-488 fluorescent dye. In PC3 cells expressing mCherry-Cavin1, Transferrin positive endosomes showed little overlap with full-length mCherry-Cavin1-positive spots on the cell surface (**Fig. S9**). However, the mCherry-Cavin1-ΔDR1 construct formed intracellular clusters with transferrin positive endosomes surrounding them similar to EEA1. These large intracellular structures were then visualised by APEX labelling and electron microscopy imaging [54] of GFP-Cavin1-ΔDR1 in PC3 cells, revealing intracellular assemblies consisting of large clusters of vesicles with a surrounding halo of GFP-Cavin1-ΔDR1 labelling **(Fig. 6E)**. In contrast, GFP-Cavin1 expression resulted in formation of the characteristic single caveolae and rosettes of caveolae at the plasma membrane as expected **(Fig. 6E)**.

We lastly performed live imaging of PC3 cells expressing either GFP-Cavin1 or GFP-Cavin1-ΔDR1 with Rab5a-mCherry as a marker of early endosomes. Caveolae are consistently localised to the trailing edge of migrating cells, where constant membrane remodelling events are occurring [55]. In migrating PC3 cells we observe dynamic GFP-Cavin1 positive caveola puncta undergoing transient fission and fusion events and kiss-and-run interactions with Rab5a-mCherry positive endosomes similar to previous observations [56] (**Fig. 6F**, **Movie S4**). In contrast, GFP-Cavin1-ΔDR1 initially showed plasma membrane puncta fusion events similar to GFP-Cavin1 (imaged at an early 12 h time point following transfection before larger immobile condensates are formed), but over time resulted in formation of the larger structures that stably associated with Rab5a positive endosomes (**Fig. 6F**, **Movie S5**). This suggests that the DR1 domain is important for the dynamics of intracellular trafficking and recycling of caveolae at endosomes. Overall, our results show that disordered sequences of Cavin1 are essential for generating caveolae, but that each DR domain has a distinct

348 function. Removing the C-terminal DR3 domain prevents interaction with CAV1 and results in mis-
349 localisation to the cytoplasm and association with microtubules. Removing the N-terminal DR1,
350 which results in gel formation and membrane clustering *in vitro,* allows initial caveola formation with
351 CAV1 at the plasma membrane, but then causes subsequent accumulation of aberrant intracellular
352 protein and membrane assemblies with a subset of early endosomes unable to recycle to the plasma
353 membrane.
354

355 **Minimal Cavin1 DR sequences needed for membrane remodelling are also essential for caveola**
356 **formation**

357 Using the series of truncations tested *in vitro* for membrane remodelling activity, we next asked if the
358 same minimal sequences are sufficient for caveola formation in cells. GFP-Cavin1(10-392) with
359 deletion of the first nine amino acids showed a relatively normal localisation with CAV1 puncta at
360 the cell surface. However, GFP-Cavin1(30-392) formed large intracellular puncta and clusters that
361 co-localised with CAV1 **(Fig. 7A),** and also showed a partial co-localisation with EEA1 (**Fig. S8C**),
362 similar to Cavin1 with the complete DR1 domain removed. Thus, deletion of the N-terminal DR1
363 sequence of Cavin1 has a progressive effect on the re-distribution of caveolae from the plasma
364 membrane to intracellular endocytic compartments.

365 The C-terminal DR3 truncation GFP-Cavin1(1-345) retained a normal ability to generate
366 plasma membrane puncta that co-localised with CAV1 (**Fig. 7A**), and APEX labelling and electron
367 microscopy of GFP-Cavin1(1-345) showed its normal localisation to caveolae at the plasma
368 membrane **(Fig. 7B)**. Further deletion of C-terminal DR3 sequences in GFP-Cavin1(1-330), however,
369 resulted in a total cytosolic redistribution. The C-terminal truncations show that amino acids (346-
370 392) are dispensable for generating caveolae in PC3 cells, while residues 330-345 are essential.
371 Finally, we used a proximity ligation assay (PLA) [10] to assess the interactions of Cavin1 C-terminal
372 truncations with CAV1 at the plasma membrane. PLA analyses correlated with the cellular imaging
373 of the GFP constructs, showing that the mutant Cavin1(1-345) can interact with (or is at least in close
374 proximity to) CAV1, while the shorter truncations Cavin1(1-330) and Cavin1(1-310) do not **(Fig.**
375 **7C; Fig. S10)**.
376

377 **Specific DR sequences are essential for the ability of Cavin1 to form caveolae**

378 The disordered sequences 1-30 and 310-345 in DR1 and DR3 are required for Cavin1 to efficiently
379 self-associate, remodel synthetic phospholipid membranes *in vitro*, and for caveola formation with
380 CAV1 in cells. To understand these sequences in more detail we generated a series of specific
381 mutations in the DR1, DR2 and DR3 domains in the context of the minimal functional construct
382 Cavin1(1-345) (**Fig. 8A**). Beginning with DR1 (residues 1-30), we first tested whether the acidic

383 amino acids were important by mutating the Glu/Asp residues to alanine (DR1mut1). When GFP-
384 tagged Cavin1(1-345) mutant DR1mut1 was expressed in PC3 cells it formed large intracellular
385 puncta and co-localised with CAV1 **(Fig. 8B).** These puncta also colocalised with a sub-population
386 of EEA1-positive endosomes, but not LAMP1 or GM130 **(Fig. S11A)**. APEX labelling and imaging
387 by EM showed clusters of GFP-Cavin1(1-345) mutant DR1mut1 that appeared identical to those
388 formed by either GFP-Cavin1-ΔDR1 or GFP-Cavin1(30-392) (**Fig. S11B**). By FCS, this variant
389 showed a significant increase in diffusivity with respect to wild-type Cavin1(1-345), indicating that
390 its net negative charge is important for self-association (**Fig. S11C**). More precise mutation of
391 Asp/Glu residues in the first ten amino acids of DR1 (mutant DR1mut2) had no effect on the ability
392 of GFP-Cavin1(1-345) to form caveolae, while altering the Asp/Glu residues in amino acids 10-30
393 of DR1 (DR1mut3) resulted in the same phenotype as mutant DR1mut1 (or complete deletion of
394 DR1), forming large intracellular clusters with CAV1 (**Fig. 8A and 8B**). We next substituted DR1(1-
395 30) with random Gly/Ser sequences, while maintaining the relative positions of acidic Asp/Glu
396 residues and prolines (DR1mut4). The objective was to determine if any other sequences apart from
397 the acidic side-chains contributed to the activity of the domain. In MCF7 cell lysates the DR1mut4
398 mutant did not show a major difference in diffusivity by FCS compared to wild-type Cavin1(1-345)
399 indicating that only the acidic side-chains in the DR1 region are necessary for self-association **(Fig.**
400 **S11C)**. The subcellular localisation of GFP-Cavin1(1-345) mutant DR1mut4 in DR1 in PC3 cells
401 also showed normal co-localisation with CAV1 at the plasma membrane **(Fig. 8B)**, indicating that it
402 is the electrostatic properties of the DR1 sequence that are most important for its function and not the
403 specific sequence itself. However, the spacing of acidic residues in DR1 is also critical, as complete
404 removal of surrounding sequences (DR1mut5) also results in GFP-Cavin1(1-345) mis-localization.
405 An analogous result was observed for the central DR2 domain of Cavin1, where mutation of the
406 acidic residues (DR2mut6) abolished caveola recruitment in PC3 cells and prevented self-association
407 in MCF7 cell lysates, while altering the surrounding sequences had no effect on caveola formation
408 (M14) (**Fig. 8C**; **Fig. S11C**). Thus the presence and the spacing of acidic sequences in DR1 and DR2
409 are essential for normal caveola formation, but their specific surrounding sequences are not.

410 Lastly, we assessed the roles of specific sequences in the essential DR3 region (residues 311-
411 345). The removal of acidic Asp/Glu residues in GFP-tagged Cavin1(1-345) (DR3mut8) resulted a
412 diffuse cytosolic localisation in PC3 cells **(Fig. 8D),** and prevented self-association in FCS
413 measurements (**Fig. S11C**). These results show that the acidic Glu/Asp residues in the Cavin1 DR1,
414 DR2 and DR3 domains are all essential for oligomeric interactions and forming caveolae with CAV1
415 at the cell surface. The acidic side-chain mutations result in identical phenotypes to the complete
416 truncation of the DR1 and DR3 domains. In contrast to the DR1 and DR2 domains however, we found
417 that in DR3 altering everything other than Asp/Glu residues (DR3mut9) resulted in a protein with a

418 normal ability to self-associate (**Fig. S11A**), but that was unable to restore caveola formation with
419 CAV1 in PC3 cells (**Fig. 8C**; **Fig. S11C**). This protein was generally cytosolic, but in some cells we
420 observed the formation of numerous spherical cytoplasmic structures, that dynamically exchange
421 with the cytosol as shown by FRAP analysis and regularly undergo fusion, suggesting the protein has
422 undergone LLPS and droplet formation (**Fig. 8E; Fig. S11D; Movie S6**). Remarkably, unlike the
423 complete DR3 deletion however, purified Cavin1(1-345) DR3mut9 is still able to remodel and
424 tubulate synthetic liposomes *in vitro* **(Fig. S11E)**. This indicates that while specific sequences in the
425 Cavin1 region 310-345 are dispensable for large scale oligomer formation, LLPS and membrane
426 remodelling, they are still essential for recruitment to caveolae with CAV1 in cells. The acidic side-
427 chains in this region, however, are required for all of these functional Cavin1 activities (mutant
428 DR3mut8). To refine this further, we designed three shorter variants of the DR3mut9 mutation,
429 DR3mut10 (311-320), DR3mut11 (321-331), and DR3mut12 (332-345). While mutant DR3mut12
430 behaved like wild-type Cavin1 and formed normal caveolae, both mutant DR3mut10 and DR3mut11
431 showed a cytosolic distribution similar to DR3mut9 (**Fig. 8D**). These results indicate that specific
432 sequences in the Cavin1 DR3 region 311-331 are strictly required for CAV1 association and caveola
433 formation, while acidic residues within DR3 region (332-345) are essential for promoting
434 electrostatic oligomeric Cavin1 assembly. Altogether, these studies demonstrate the critical
435 importance of acidic residues in all three DR domains for promoting electrostatic intermolecular
436 interactions, and show that specific sequences in Cavin1 DR3 region (311-331) necessary for Cavin1
437 to function in caveola recruitment and sculpting.
438
439
440
441

Discussion

Despite the fact that intrinsically disordered sequences are a prominent and highly conserved feature of all cavins, there have been no previous studies that explicitly addressed their functional importance. We now show that they are essential for caveola formation. In addition, they also regulate the ability of Cavin1 to self-associate and undergo LLPS. *In vitro*, Cavin1 shows the classical properties of LLPS as demonstrated by phase separation that is sensitive to protein concentration, ionic strength, molecular crowding agents, and by the rapid exchange of protein in Cavin1 droplets as shown by FRAP. The sensitivity of this LLPS to salt concentration indicates an electrostatically driven Cavin1 condensation. We demonstrate the distinct roles of the disordered DR domains of Cavin1 in LLPS behaviour, including a mutant protein lacking the DR1 domain that still self-associates but no longer shows the dynamic exchange properties of the full-length protein. In addition, CAV1 was also able to associate with Cavin1 liquid droplets, an interaction that is dependent on their mutual disordered sequences. Our cellular studies show that acidic residues in all three Cavin1 disordered sequences (DR1, DR2 and DR3) are essential for generating caveolae with CAV1 at the plasma membrane. Deletion or mutation of these regions in Cavin1 result in mis-localisation and an inability to form plasma membrane caveola invaginations. Interestingly the N- and C-terminal sequences play divergent roles in this process. Deletion of the N-terminal DR1 domain affects caveola dynamics and leads to the formation of large intracellular clusters of Cavin1, CAV1, and endosomal membrane vesicles. In contrast, deletion of the DR3 domain prevents CAV1 association and results in dynamic microtubule association or cytoplasmic droplet formation. We speculate that Cavin1-ΔDR3 association with microtubules may share mechanistic similarities with the condensation of Tau on microtubules [57, 58], or interactions of multivalent positively-charged peptides with the C-terminal acidic tails of tubulin subunits [59], but this will require further study.

To better appreciate and visualise the role of the disordered DR domains in Cavin1 activity, we constructed a theoretical structural model of the protein, building on the assumption that the fundamental Cavin1 unit is a homotrimer based on the coiled-coil structure of its N-terminal HR1 domain [11] (see Materials and Methods) (**Fig. 9A**). This model points to several interesting features of the Cavin1 protein. Firstly, the combined DR1, DR2 and DR3 domains account for more than 50% of the total Cavin1 sequence. In other words, Cavin1 is not a typical globular protein but rather consists of large random-coil elements tethered by α-helical structural cores. Secondly, as suggested by sequence analyses (**Fig. S1**), there is a distinctive electrostatic pattern to the structure, with the α-helical domains providing positively charged surfaces for membrane association, and the disordered regions having a generally negatively-charged nature. A likely consequence of this is that electrostatic repulsion will cause these DR domains to orient outwards when Cavin1 is in contact with membranes, and we propose they will also form transient electrostatic interactions with the HR domains of

477 neighbouring Cavin1 molecules (**Fig. 9B**). Notably, multiple theoretical and experimental studies
478 have shown that the sequence specific electrostatically-driven interactions between disordered
479 regions can lead to LLPS and high affinity protein complex formation under physiological conditions,
480 with the tendency to phase separate (or undergo complex coacervation) increasing as the 'blockiness'
481 of the charge distribution increases [60-65].

482 Our studies of the DR domains of Cavin1 confirm that the acidic residues within these
483 domains are essential for the formation of caveolae in cells and promotion of membrane remodelling
484 *in vitro*. By what mechanism might the DR domains contribute to these membrane sculpting
485 activities? Several recent studies have demonstrated the ability of intrinsically disordered sequences
486 to generate membrane curvature when coupled to membrane binding domains [50, 66-68]. This is caused
487 by molecular crowding of the disordered sequences leading the proteins to partition with curved or
488 convex membranes so as to increase their conformational entropy; and this can also be enhanced by
489 electrostatic repulsive forces both between the disordered domains and the disordered domains and
490 the membrane itself (**Fig. 9C**). One possible mechanism we can propose for Cavin1-driven membrane
491 curvature is that negatively charged DR sequences and positively charged HR regions of Cavin1
492 combine to promote self-association, membrane interaction and protein crowding at the membrane
493 surface leading to subsequent membrane bending. In the absence of CAV1 and at high protein
494 concentrations *in vitro*, or under certain conditions in cells, Cavin1 can generate arrays of protein
495 oligomers to form membrane tubules. Under normal conditions however, the process of generating
496 membrane curvature is tightly regulated by CAV1, EHD2 and Pacsin2, and also specific membrane
497 lipids, to restrict Cavin1 remodelling activity only to caveolae. We see an almost complete correlation
498 between the ability of different Cavin1 truncations and mutants to tubulate membranes *in vitro* and
499 the ability to form caveolae *in situ*. The notable exception to this is that alteration of sequences in the
500 DR3 region 310-331 still allows Cavin1 to assemble into oligomers and efficiently tubulate synthetic
501 membranes, but result in a failure to generate caveolae in cells. This implies these specific sequences
502 in the Cavin1 DR3 region are additionally required for Cavin1 recruitment to CAV1-positive
503 membrane domains through interactions with the disordered CAV1 N-terminus.

504 A second mechanism suggested by our results (and not mutually exclusive with a role for
505 molecular crowding) is the formation of phase-separated Cavin1 domains that incorporate CAV1 at
506 the membrane itself. Intrinsically disordered regions of proteins have gained significant attention for
507 their ability to promote LLPS, or biomolecular condensation, with important biological functions
508 such as stress granule formation, assembly of nuclear sub-structures and sensing changes in cellular
509 homeostasis [19, 69]. The plasma membrane and surfaces of intracellular compartments including the
510 ER and lysosomes have been found to play a role in LLPS, acting as sites of droplet nucleation or as
511 platforms for transport of phase-separated assemblies for example [23-34]. It has also recently been

512 proposed that biomolecular condensates associated with phospholipid membranes might possess
513 emergent mechanical properties that can result in membrane curvature generation [35-37]. This is
514 depicted in schematic form in **Fig. 9D**. Here we have shown for the first time that purified Cavin1
515 can readily undergo LLPS under near physiological conditions and is able to recruit CAV1 through
516 interactions involving LLPS. The DR1 and DR3 domains contribute to this process, although neither
517 domain is strictly essential. Indeed, mutations in DR3 that prevent CAV1 interaction at the plasma
518 membrane typically promote GFP-Cavin1 liquid droplet formation in cells. Notably, removal of the
519 DR1 domain results in apparent gel formation rather than liquid droplet assembly *in vitro*, and within
520 cells results in a striking accumulation of large intracellular structures that also contain CAV1. These
521 are formed by endocytic redistribution of caveola structures from the cell surface and accumulation
522 with early endosomal membranes. Caveolae, positive for both CAV1 and Cavin1, have been shown
523 to bud from the plasma membrane and fuse with early endosomal compartments [70-75], and this would
524 almost certainly require dynamic remodelling of the protein coat to allow the fusion process to occur.
525 We postulate that the intracellular structures we observe with Cavin1-ΔDR1 are formed by
526 internalised caveolae, which have become blocked during the stage of early endosomal fusion. This
527 may be due to the DR1-truncated Cavin1 being unable to undergo normal dynamic exchange, as
528 suggested by its gel-forming properties and its propensity to cluster membrane vesicles, causing
529 inhibition or slowing of the docking/fusion with the early endosome in a process involving EEA1 and
530 Rab5a [74, 76].

531 Our data indicates that the assembly of caveolae by Cavin1 strictly depends on a 'fuzzy'
532 network of interactions promoted by electrostatic associations, with an essential role for the
533 intrinsically disordered DR domains of Cavin1 in self-association, CAV1 interaction, membrane
534 remodelling and ultimately caveola formation. Fuzzy interactions are defined broadly as those that
535 involve dynamic, exchanging, multivalent interactions with varying degrees of protein disorder or
536 structural ambiguity [77-79]. This provides versatility and reversibility in protein-protein interactions,
537 and such fuzzy interactions are also proposed to be a driver of protein phase transitions [19]. One of the
538 historically consistent observations regarding caveolae is that they do not possess an obvious or
539 highly ordered coat morphology akin to clathrin or COP-coated vesicles. Our model for caveola
540 assembly and structure differs markedly from other classical membrane coats such as clathrin or
541 COPI and COPII, which are built from symmetrical arrays of structured protein domain interactions.
542 In previous studies of caveola architecture it is notable that while some recurring structures are
543 observed, the general appearance of the caveola surface is extremely heterogeneous [47-49, 80]. While
544 structural elements of cavins and caveolins will likely produce semi-regular spacings between the
545 building blocks, the flexible nature of the disordered domains that provide the glue for caveola
546 assembly mean that the overall organisation of the coat will be highly dynamic. Caveola formation is

547 the result of multiple low affinity fuzzy interactions between Cavin1, CAV1 and membrane lipids,
548 and we propose that this leads to a metastability in caveola structure that is important in both the
549 dynamic cycling of caveolae through the endocytic pathway and also for their ability to respond to
550 stresses by rapid disassembly.
551

552

553 **Materials and methods**

554 **Cell lines maintenance and materials**

555 PC3 cells were maintained in RPMI medium (Gibco® Life technologies) supplemented with 10%
556 fetal bovine serum (FBS) and Penicillin/Streptomycin. Cell lines were sourced from ATCC and tested
557 fortnightly for mycoplasma contamination. For all experiments, 2 X 10^5 PC3 or MCF7 cells were
558 plated in either 6 well culture dishes (Nunc™, Cat. No. 140675, Culture area - 9.6 cm^2) or glass
559 bottom 35 mm dishes (ibidi, No. 1.5 glass coverslip bottom Cat No. 81218) or 35mm tissue culture
560 dishes (TPP® 93040, culture area - 9.2 cm^2). Antibodies used were as follows, rabbit polyclonal anti-
561 Caveolin1 (BD Transduction Laboratories, Cat. No. 610060), mouse monoclonal anti-GFP (Roche
562 Diagnostics Cat. No. 11814460001), Donkey anti-Rabbit IgG (H+L) Secondary Antibody Alexa
563 Fluor® 555 conjugate (Thremo Fisher Scientific, Cat No. A31572). Mouse monoclonal anti-tubulin
564 (Anti-alpha Tubulin antibody [DM1A] - Abcam (ab7291)). Folch lipids were obtained from Sigma
565 Aldrich Folch I fraction (B1502)

566

567 **Molecular cloning and plasmids**

568 For Recombinant protein expression in *E. coli* two vectors (pHUE and pOPINE-GFP) were used to
569 generate Cavin1 DR domain variants summarised in **Fig. S1**. pHUE vector was used to generate N-
570 terminal 6X-Histidine-Ubiquitin tagged DR domain variants of Cavin1 using overlap extension
571 polymerase chain reaction (OE-PCR) technique at SacII restriction enzyme site [82]. GFP tagged cavin
572 DR domain variants were generated using pOPINE-GFP vector (in house vector with pOPINE
573 backbone containing GFP) BamHI restriction enzyme site with N-terminal 6X-Histidine-Ubiquitin
574 tag and C-terminal GFP tag using OE-PCR [83]. For mammalian cell expression constructs, eGFPC1
575 and eGFPN1 vectors were used to generate respective DR domain Cavin1 mutants summarised in
576 **Fig. S2**. Specific Cavin1 (1-345) DR domain genes (summarised in **Fig. 8A**) and all mCherry tagged
577 CAV1 genes were artificially synthesized (Gene Universal) and selective genes were subsequently
578 cloned into eGFPC1 and pHUE vectors using OE-PCR for mammalian and bacterial expression
579 respectively.

580

581 **Recombinant protein expression and purification**

582 Recombinant protein expression was performed using *Eschericia coli* strain Rosetta™ 2 (DE3)
583 (Novagen) (Merck Cat. No 71403). Protein expression was always performed using freshly
584 transformed chemically competent *E. coli* Rosetta 2 cells with respective plasmids. Cell were
585 propogated in either LB or TB media and protein expression was performed by inducing with 0.5
586 mM IPTG (Isopropyl ß-D-1-thiogalactopyranoside, Bioline, Cat No. BIO-37036) overnight at 18^0C.

587 Next day, cells were harvested in 20 mM HepesKOH (pH 7.6), 500 mM NaCl (500GF buffer) with
588 addition of benzamidine hydrochloride (Sigma Aldrich, B6506) and cOmplete™, EDTA-free
589 Protease Inhibitor Cocktail Roche (Sigma Aldrich, 4693132001). Cleared cell lysates were prepared
590 using a continuous flow cell disruptor (Constant Systems Limited, UK) at pressure range 25 – 30 kPsi
591 with subsequent addition of 0.5 % w/v Triton X-100 (Cavin1 purification) or n-dodecyl β-D-
592 maltoside (DDM) (1.2 mM) (MBP-GBP-CAV1 purification) and 5 mM imidazole (Sigma Aldrich,
593 792527) followed by centrifugation 35,000x *g* for 30 min. Purification of 6X-Histidine tagged cavin
594 proteins was done using TALON metal affinity resin (ClonTech, Scientifix Cat No. 635503). Talon
595 resin was thoroughly washed with 500GF buffer containing 5 mM imidazole to remove detergent and
596 non-specifically bound proteins, and elution was performed in 500GF buffer containing 300 mM
597 imidazole. Protein samples were immediately loaded on size exclusion chromatography column
598 Superose 6 10/30GL pre-equilibrated with 20 mM HepesKOH pH7.6, 150 mM NaCl (150GF buffer)
599 or 150GF buffer with 1.2mM DDM detergent. Size exclusion profiles of purified Cavin truncation
600 mutants are shown in **Fig. S11**. The purified protein used in assays (marked with arrows) appears to
601 be slightly truncated but forms part of megadalton size full length protein complex eluting in higher
602 molecular weight fractions (**Fig. S11**). This partial truncation can be due to presence of multiple
603 protease sensitive PEST (proline, glutamate, serine, threonine) regions in DR sequences of Cavin1 [9].
604 There has been evidence for the presence of truncated species of Cavin1 bound to native caveolae in
605 cells suggesting that this might be an inherent property of this protein regardless of its source of
606 expression [7, 84].

607 Purification of mammalian Cavin1 was performed by Transfecting GFP-tagged Cavin1 using
608 polyethylenimine (PEI) transfection reagent (Sigma-Aldrich Cat. No. 408727) with 1:4 w/w ratio
609 (DNA:PEI) and cells were harvested 24 h post-transfection. Cell lysis was performed in 20 mM
610 Hepes-KOH pH 7.6, 500 mM NaCl buffer containing 1% Triton X-100 with three times 3-s
611 sonication pulse at output power 10. Lysate was then centrifuged at 5,000X g for 10 min, and
612 supernatant fraction was incubated with purified GFP nanobody tagged with MBP for 30 min at 4°C.
613 Finally, lysate nanobody mixture was incubated with amylose resin (NEB Cat No. E8021L) for 2 h
614 at 4°C. Amylose resin was then extensively washed with 20 mM Hepes-KOH pH 7.6, 500 mM NaCl
615 buffer containing 1% Triton X-100, and elution was performed in 20 mM Hepes-KOH pH 7.6, 500
616 mM NaCl buffer containing 20 mM Maltose (Sigma-Aldrich Cat. No. M2250). Elute was
617 concentrated with subsequent addition of Prescission protease to remove MBP tag and finally loaded
618 on Superose 6 10/ 30GL size exclusion column equilibrated in 20 mM Hepes-KOH pH 7.6, 150 mM
619 NaCl. Concentration of gel filtration elute was avoided as it leads to precipitation in lower salt
620 content.

621

622 **Fluorescence correlation spectroscopy (FCS) analysis**

623 FCS analysis was performed on a Zeiss LSM 710 confocal microscope equipped with 40x/1.2W C-
624 Apo lens and twin BiG GaAsP detectors capable of single molecule detection. Briefly, MCF7 cells
625 were lysed in a buffer (200 µl) containing 25 mM Tris (pH 7.4), 150 mM NaCl while passing through
626 a 27G needle 6 times. Lysates were then centrifuged at 17,000x g for 10 min to remove cell debris.
627 Supernatant was then used for FCS analysis. Purified GFP tagged cavin proteins were prepared for
628 FCS by dilution of respective stock solutions of cavin truncates in either 500GF or 150GF buffer to
629 achieve 0.1 µM protein concentration with subsequent centrifugation at 17,000 X g for 10 min. At
630 the beginning of each FCS session on a Zeiss LSM 710, pinhole calibration was done with BODIPY-
631 FL maleimide dye (Cat. No. B30466). Subsequently, diffusion time for three dyes that differ in
632 molecular weight and particle size BODIPY-FL maleimide (~24 µs), BODIPY-FL iodoacetamide
633 (~22 µs) and TAMRA DIBO (~37 µs) was measured for each session (**Fig. S11I**). FCS measurement
634 for each GFP tagged Cavin protein was then done for 10 s and repeated 10 times with a binning time
635 of 200 ns. FCS measurements showing presence of aggregates were removed from analysis. The
636 autocorrelation function $G(\tau)$ was fitted using a predefined isotropic 3D translational diffusion $G_d(\tau)$
637 model from the ConFoCor model tool with fixed amplitude (A) and structural parameter, $G(\tau) = 1 +$
638 $A * G_d(\tau)$. The diffusion coefficient or diffusivity ($\mu s^2 Sec^{-1}$) for each measurement was exported from
639 the Zeiss analysis program and plotted for all constructs in Graph pad Prism software. Hydrodynamic
640 radius calculations were done using Stokes-Einstein equation with basic assumption of perfect
641 spherical object diffusion. Stokes – Einstein equation; $D = K_B T/6\pi nr$, Where, K_B – Boltzmann
642 constant, T – Temperature (298K), π – pi (3.14), n – dynamic viscosity (Pa.S) and r – hydrodynamic
643 (Stokes) radius of spherical particle.

644

645 **In vitro phase separation assays**

646 Purified GFP-tagged Cavin1 proteins, or mixtures of mCherry-CAV1 and GFP-Cavin1 proteins, were
647 diluted to respective protein and/or salt concentrations prior to addition of dextran T-500 (Pharmacia).
648 Dextran solution was added on the top of protein solution without any mixing to allow natural
649 diffusion of dextran. Image acquisition and fluorescence recovery after photobleaching (FRAP)
650 assays were performed after 2 min wait period to allow phase separated droplets to settle. Phase
651 separation analysis was done within 10 min post addition of dextran. Non-bleaching image
652 acquisition conditions were established before performing FRAP assay. FRAP analysis was done by
653 bleaching rectangular area (2 µm X 1 µm approximately) within protein droplet using 488 nm Argon
654 laser and subsequent image acquisition was done one frame per second. Recovery curves from
655 different proteins were normalised without acquisition bleaching correction using formula $[F_{(T)} -$
656 $F_{(postbleachT=0)}]/[F_{(Prebleach)} - F_{(postbleachT=0)}]$. Normalised data points were used to perform non-linear

657 exponential recovery fit using equations within ImageJ 1.50g or Prism version 8 to obtain half-life
658 value for fluorescence recovery of respective protein.
659
660
661 **Liposome preparation and in vitro membrane tubulation assay**
662 Liposomes were prepared by mixing of 10 µL 10 mM stock solution of Folch lipids (bovine brain
663 extract lipid - Folch I fraction Sigma Aldrich B1502) with 50 µL chloroform in a round-bottom flask.
664 The mixtures were dried gently by a stream of nitrogen first and under vacuum overnight thereafter.
665 Liposomes were rehydrated in 500 µL 150GF buffer followed by repetitive freeze-thaw cycles for 3
666 – 5 times, using first a mixture of dry ice and acetone followed with 60°C water. The liposomes were
667 then extruded through a 400-nm polycarbonate membrane 21 times using an Avanti mini-extruder to
668 generate large unilamellar lipid vesicles (LUVs).
669 A 5 µl volume of purified Cavin1 variants [~ 0.1 mg/ml (1.5 – 2 µM)] was mixed with 5 µl
670 200 µM liposomes for 1 – 3 min at room temperature. Samples were then quickly spotted onto
671 formvar-carbon coated electron microscopy grids (Cu/Pd grids 200 mesh hexagonal – ProSciTech -
672 GCU-PD200H) for 10 s and excess samples were removed by blotting at corner using Whatman filter
673 paper. This is followed by 2 - 3 distilled water washes in similar fashion and subsequent application
674 of 1% uranyl acetate stain. The excess of stain was removed by blotting and grids were allowed to air
675 dry for a while before viewing under the electron microscope. Final images were acquired on JEOL
676 1011 electron microscope at 80 kV.
677
678 **Giant multilamellar vesicle (GMV) experiments**
679 Giant multilamellar vesicles (GMV) were prepared using electro-formation method described
680 before[85]. Briefly, lipids mixture dissolved in chloroform / methanol solution was gently applied to
681 indium-tin-oxide coated glass slide (Sigma Aldrich Cat. No. 636908) as multiple layers. This solution
682 was then dried under constant stream of nitrogen to remove organic solvent and further dried under
683 vacuum overnight. Next day, electro-formation was performed at 50^0C in 150GF buffer for 1 hr.
684 Vesicles were used immediately for experiments.
685
686 **Cryoelectron microscopy / tomography of Cavin1 coated membrane tubules**
687 Liposome tubulation reaction was assembled as described in the previous section and subjected to
688 vitrification after a 1 – 3 min incubation period. For vitrification, the sample was applied to Lacey
689 carbon grids (EMS, Hatfield, PA,USA) using a Vitrobot Mark II (FEI, Eindhoven, NL) plunge freezer
690 with 4 µl of sample, 6 s blotting time and a -3 mm offset at 24^0C and 100% humidity. Images were
691 collected on a Tecnai G2 F30 TEM (FEI, Eindhoven, NL) operated at 300 kV at a magnification of

692 12,000X with 5 µm defocus. Images were recorded on a Gatan K2 summit camera in counting mode
693 for a final pixel size of 3.556 Å per pixel. Images were processed in either IMOD (version 4.9) or
694 ImageJ.
695 Tilt-series were acquired on a Talos Arctica TEM (Thermo Fisher Scientific-FEI, Eindhoven,
696 NL) operated at 200 kV and at a magnification of 45,000x (final pixel size 3.11 Å per pixel). Images
697 were recorded using the microscope software Tomography (Thermo Fisher Scientific-FEI, NL) on
698 Falcon 3 (Thermo Fisher Scientific-FEI, NL) camera operated in counting mode at an angular range
699 of -60^0 to 60^0 in a bidirectional fashion and at an angular increment of 2º. The defocus was set to -5
700 µm. Unbinned movies of 8 frames with a set dose rate of ~1.7 e/$Å^2$ were acquired and tomographic
701 reconstructions were generated using the weighted back-projection method in IMOD
702 (https://bio3d.colorado.edu/imod/ version 4.9).
703
704 **Electron microscopy processing of PC3 cells**
705 PC3 cells were plated onto 30 mm tissue culture dishes and allowed to adhere to dishes for 48 h prior
706 to transfection. Cells were then co-transfected with APEX-GBP and respective cavin1 mutant
707 constructs. 24 h post transfection, cells were fixed with 2.5% glutaraldehyde in 0.1 M sodium
708 cacodylate buffer (cacodylate) (pH7.4) for 1 h. DAB (3'3-diaminobenzidine tetrahydrochloride,
709 Sigma-Aldrich Cat. No. D5905) reaction was then performed as follows. Briefly, cells were washed
710 with DAB/cacodylate mixture (DAB final concentration – 1 mg/ml) for 2 mins, then treated with
711 DAB/cacodylate + 5.88 mM H_2O_2 (hydrogen peroxide, Sigma-Aldrich Cat. No. H1009) for 20 mins.
712 Cells were then washed with 0.1 M sodium cacodylate buffer and contrasted with 1% osmium
713 tetroxide for 2 mins. Cells were then embedded in LX112 resin and thin sections were cut as described
714 previously [54]. Images were acquired on JEOL 1011 electron microscope fitted with a Morada CCD
715 camera (Olympus) under the control of iTEM software and operated at 80kV.
716 .
717
718 **Immunofluorescence analysis, live cell imaging and Proximity ligation assay (PLA)**
719 PC3 cells were grown at about ~50% confluency in RPMI 1640 medium supplemented with 10%
720 FBS. Cells were then transfected with respective Cavin1 mutants using Lipofectamine 3000
721 (Invitrogen) as per manufacturer's instructions. Cells were fixed 24 h post transfection with 4%
722 paraformaldehyde in phosphate-buffered saline (PBS) at 4ºC and subsequently permeabilised with
723 0.1% Triton X-100 in PBS for 7 mins. Cells were probed with CAV1 antibody (Dilution 1:600) and
724 anti-Rabbit secondary antibody Alexa Fluor® 561 conjugate (Dilution 1:400). For Transferrin uptake
725 assays, PC3 cells expressing either GFP-Cavin1 or GFP-Cavin1-ΔDR1 were incubated with
726 transferrin labelled with Alexa-488 (5 µg/ml) for 1h at 37 ºC. Cells were then washed three times

727 with ice cold PBS and cell were subsequently fixed with 4% paraformaldehyde in PBS for all
728 experiments except live imaging. Cholesterol addition experiments were performed in MCF7 cells
729 expressing GFP tagged Cavin1 with serum starvation (Serum free DMEM + 1% BSA, 1h) prior to
730 the addition of water soluble analog of Cholesterol (Sigma-Aldrich Cat. No. C4951). Cells were
731 incubated in DMEM media containing Cholesterol for 40 min at 37ºC with immediate fixation using
732 4% paraformaldehyde in phosphate-buffered saline (PBS) at room temperature. Confocal images
733 (1024X1024) were acquired on Zeiss inverted LSM 880 coupled with fast airyscan detector (Carl
734 Zeiss, Inc) equipped with 63X oil immersion objective, NA 1.4. Images were acquired at different
735 laser power for GFP tagged truncation mutants and detector gain settings in order to avoid
736 oversaturation of pixels. All images were processed for brightness/contrast (histogram) adjustment
737 for visualisation using ImageJ. For live cell imaging and FRAP analysis, cells were plated on glass
738 bottom (No. 1.5) petri dishes (ibidi) and allowed to grown at about ~70% confluency and transfected
739 with respective Cavin1 mutants. For bleaching, 488 nm laser at 100% attenuation power was used
740 for 20 iterations and subsequent imaging was done at one frame per second. Airyscan processing was
741 done automatically in Zeiss software (ZEN 2.3). For PLA, PC3 cells were processed as described
742 previously [10]. Images were then acquired on Zeiss LSM 710 and LSM 880 confocal microscope (Carl
743 Zeiss, Inc) equipped with 63X oil immersion objective and quantitation of PLA dots per cell was
744 performed using find maxima function in ImageJ with offset of 25.
745
746 **Constructing a structural model of mouse Cavin1**
747 A structural model of mouse Cavin1 was built manually based both known structures of the mouse
748 Cavin1 HR1 domain [11] (PDB ID 4QKV), the previous model of the Cavin1 undecad UC1 region [10],
749 and secondary structure prediction of the Cavin1 protein carefully cross-referenced to several Cavin1
750 homologues and other Cavin family members [11]. Based on the homotrimeric coiled-coil structure of
751 the HR1 domain we constructed our model under the assumption that a single Cavin1 'unit' would
752 consist of three identical Cavin1 chains. The secondary structure predictions and previous crystal
753 structure led us to define the following regions of Cavin1 as either α-helical or random-coil; DR1,
754 residues 1-48, random-coil; HR1, residues 49-147, α-helical (based on PDB 4QKV of mouse Cavin1
755 HR1); DR2, residues 148-218, random-coil; HR2, α-helical for residues 219-242, random-coil for
756 residues 243-244, α-helical for residues 245-278 (model from [10]), random-coil for residues 279-286,
757 α-helical for residues 287-297; DR3, residues 298-392, random coil. Stretches of random-coil were
758 built and added to α-helical domains manually in COOT Version 0.8.2 [86], and the final model was
759 subjected to simple geometry regularisation in PHENIX Version 1.14 [87]. Structural images and
760 electrostatic surface representations were rendered with PYMOL Version 2.3.1.
761

762 **Statistical analyses**

763 Statistical analysis and P value calculations were performed by one-way ANOVA using graph pad
764 Prism software.

765

766

767 **Acknowledgements**

768 This work was supported by grants from the National Health and Medical Research Council of
769 Australia (NHMRC) (to RGP grant number APP569542 and APP1037320) and the Australian
770 Research Council (ARC) (to BMC, grant number DP120101298). RGP is supported by an NHMRC
771 Senior Principal Research Fellowship from the NHMRC (APP1058565) and by the Australian
772 Research Council Centre of Excellence in Convergent Bio-Nano Science and Technology (R.G.
773 Parton). BMC is supported by an NHMRC Senior Research Fellowship (APP1136021). Confocal
774 microscopy was performed at the Australian Cancer Research Foundation (ACRF)/Institute for
775 Molecular Bioscience (IMB) Dynamic Imaging Facility for Cancer Biology, established with funding
776 from the ACRF. The authors acknowledge the use of the Cryo Electron Microscopy Facility through
777 the Victor Chang Innovation Centre, funded by the NSW government, and the Electron Microscope
778 Unit within the Mark Wainwright Analytical Centre at UNSW Sydney.

779

780

781 **Author contributions**

782 BMC and RGP conceived the project, study and acquired funding. VT performed molecular cloning,
783 in vitro protein purification, in vitro, cellular assays, live imaging and FCS experiments. GY assisted
784 in molecular cloning and in vitro protein purification. KAM assisted in cellular and phase separation
785 assay. OK performed preliminary FCS analysis of cavins in the eukaryotic Leishmania terentolae cell
786 free lysate system. NC initiated cholesterol addition experiments completed by VTJR performed
787 transferrin uptake assay, cellular processing for electron microscopy and electron microscopy image
788 acquisition. NA and MF performed tomography data acquisition, and trained VT in cryo-EM
789 methods. All authors commented on the manuscript. VT, RGP and BMC wrote the manuscript.

790

791 **Conflict of interest**

792 Authors declare that they have no conflict of interest.

793

794

795

796 **References**

797

798 1. Lamaze, C., Tardif, N., Dewulf, M., Vassilopoulos, S. & Blouin, C.M. The caveolae dress
799 code: structure and signaling. *Current Opinion in Cell Biology* **47**, 117-125 (2017).

800 2. Parton, R.G. & del Pozo, M.A. Caveolae as plasma membrane sensors, protectors and
801 organizers. *Nature reviews. Molecular cell biology* **14**, 98-112 (2013).

802 3. Parton, R.G. Caveolae: Structure, Function, and Relationship to Disease. *Annual Review of*
803 *Cell and Developmental Biology* **34**, 111-136 (2018).

804 4. Hayer, A., Stoeber, M., Bissig, C. & Helenius, A. Biogenesis of caveolae: stepwise assembly
805 of large caveolin and cavin complexes. *Traffic* **11**, 361-382 (2010).

806 5. Ariotti, N. *et al.* Molecular Characterization of Caveolin-induced Membrane Curvature. *J Biol*
807 *Chem* **290**, 24875-24890 (2015).

808 6. Busija, A.R., Patel, H.H. & Insel, P.A. Caveolins and cavins in the trafficking, maturation,
809 and degradation of caveolae: implications for cell physiology. *Am J Physiol Cell Physiol* **312**,
810 C459-C477 (2017).

811 7. Hill, M.M. *et al.* PTRF-Cavin, a conserved cytoplasmic protein required for caveola formation
812 and function. *Cell* **132**, 113-124 (2008).

813 8. Walser, P.J. *et al.* Constitutive formation of caveolae in a bacterium. *Cell* **150**, 752-763
814 (2012).

815 9. Bastiani, M. *et al.* MURC/Cavin-4 and cavin family members form tissue-specific caveolar
816 complexes. *The Journal of cell biology* **185**, 1259-1273 (2009).

817 10. Tillu, V.A. *et al.* A variable undecad repeat domain in cavin1 regulates caveola formation and
818 stability. *EMBO reports* **19**, e45775 (2018).

819 11. Kovtun, O. *et al.* Structural insights into the organization of the cavin membrane coat
820 complex. *Developmental cell* **31**, 405-419 (2014).

821 12. Kovtun, O., Tillu, V.A., Ariotti, N., Parton, R.G. & Collins, B.M. Cavin family proteins and
822 the assembly of caveolae. *Journal of Cell Science* **128**, 1269-1278 (2015).

823 13. Mohan, J., Moren, B., Larsson, E., Holst, M. & Lundmark, R. Cavin3 interacts with cavin1
824 and caveolin1 to increase surface dynamics of caveolae. *J Cell Sci* (2015).

825 14. Gambin, Y. *et al.* Single-molecule analysis reveals self assembly and nanoscale segregation
826 of two distinct cavin subcomplexes on caveolae. *eLife* **3**, e01434 (2014).

827 15. Oates, M.E. *et al.* D2P2: database of disordered protein predictions. *Nucleic Acids Research*
828 **41**, D508-D516 (2012).

829 16. Banks, D.S. & Fradin, C. Anomalous diffusion of proteins due to molecular crowding.
830 *Biophys J* **89**, 2960-2971 (2005).

831 17. Lavie, Y., Fiucci, G. & Liscovitch, M. Up-regulation of caveolae and caveolar constituents in
832 multidrug-resistant cancer cells. *J Biol Chem* **273**, 32380-32383 (1998).

833 18. Tillu, V.A., Kovtun, O., McMahon, K.A., Collins, B.M. & Parton, R.G. A phosphoinositide-
834 binding cluster in cavin1 acts as a molecular sensor for cavin1 degradation. *Mol Biol Cell* **26**,
835 3561-3569 (2015).

836 19. Boeynaems, S. *et al.* Protein Phase Separation: A New Phase in Cell Biology. *Trends Cell*
837 *Biol* **28**, 420-435 (2018).

838 20. Boyko, S., Qi, X., Chen, T.H., Surewicz, K. & Surewicz, W.K. Liquid-liquid phase separation
839 of tau protein: The crucial role of electrostatic interactions. *J Biol Chem* **294**, 11054-11059
840 (2019).

841 21. Gomes, E. & Shorter, J. The molecular language of membraneless organelles. *J Biol Chem*
842 **294**, 7115-7127 (2019).

843 22. Wang, J. *et al.* A Molecular Grammar Governing the Driving Forces for Phase Separation of
844 Prion-like RNA Binding Proteins. *Cell* **174**, 688-699 e616 (2018).

845 23. Alenquer, M. *et al.* Influenza A virus ribonucleoproteins form liquid organelles at
846 endoplasmic reticulum exit sites. *Nat Commun* **10**, 1629 (2019).

847 24. Case, L.B., Zhang, X., Ditlev, J.A. & Rosen, M.K. Stoichiometry controls activity of phase-
848 separated clusters of actin signaling proteins. *Science* **363**, 1093-1097 (2019).

849 25. Ditlev, J.A. *et al.* A composition-dependent molecular clutch between T cell signaling
850 condensates and actin. *eLife* **8** (2019).

851 26. Huang, W.Y.C. *et al.* A molecular assembly phase transition and kinetic proofreading
852 modulate Ras activation by SOS. *Science* **363**, 1098-1103 (2019).

853 27. Johnson, A. *et al.* TFG clusters COPII-coated transport carriers and promotes early secretory
854 pathway organization. *EMBO J* **34**, 811-827 (2015).

855 28. Liao, Y.C. *et al.* RNA Granules Hitchhike on Lysosomes for Long-Distance Transport, Using
856 Annexin A11 as a Molecular Tether. *Cell* **179**, 147-164 e120 (2019).

857 29. Ma, W. & Mayr, C. A Membraneless Organelle Associated with the Endoplasmic Reticulum
858 Enables 3'UTR-Mediated Protein-Protein Interactions. *Cell* **175**, 1492-1506 e1419 (2018).

859 30. Milovanovic, D., Wu, Y., Bian, X. & De Camilli, P. A liquid phase of synapsin and lipid
860 vesicles. *Science* **361**, 604-607 (2018).

861 31. Snead, W.T. & Gladfelter, A.S. The Control Centers of Biomolecular Phase Separation: How
862 Membrane Surfaces, PTMs, and Active Processes Regulate Condensation. *Mol Cell* **76**, 295-
863 305 (2019).

864 32. Zappa, F. *et al.* The TRAPP complex mediates secretion arrest induced by stress granule
865 assembly. *EMBO J* **38**, e101704 (2019).

866 33. Beutel, O., Maraspini, R., Pombo-García, K., Martin-Lemaitre, C. & Honigmann, A. Phase
867 Separation of Zonula Occludens Proteins Drives Formation of Tight Junctions. *Cell* **179**, 923-
868 936.e911 (2019).

869 34. Schwayer, C. *et al.* Mechanosensation of Tight Junctions Depends on ZO-1 Phase Separation
870 and Flow. *Cell* **179**, 937-952.e918 (2019).

871 35. Bergeron-Sandoval, L.P. & Michnick, S.W. Mechanics, Structure and Function of
872 Biopolymer Condensates. *J Mol Biol* **430**, 4754-4761 (2018).

873 36. Lacy, M.M., Ma, R., Ravindra, N.G. & Berro, J. Molecular mechanisms of force production
874 in clathrin-mediated endocytosis. *FEBS Lett* **592**, 3586-3605 (2018).

875 37. Bergeron-Sandoval, L.-P. *et al.* Endocytosis caused by liquid-liquid phase separation of
876 proteins. *bioRxiv* **145664** (2017).

877 38. Li, Y., Lipowsky, R. & Dimova, R. Membrane nanotubes induced by aqueous phase
878 separation and stabilized by spontaneous curvature. *Proc Natl Acad Sci U S A* **108**, 4731-4736
879 (2011).

880 39. Alberti, S. *et al.* A User's Guide for Phase Separation Assays with Purified Proteins. *J Mol*
881 *Biol* **430**, 4806-4820 (2018).

882 40. Wang, Z., Zhang, G. & Zhang, H. Protocol for analyzing protein liquid–liquid phase
883 separation. *Biophysics Reports* **5**, 1-9 (2019).

884 41. Itzhak, D.N., Tyanova, S., Cox, J. & Borner, G.H. Global, quantitative and dynamic mapping
885 of protein subcellular localization. *eLife* **5** (2016).

886 42. Molliex, A. *et al.* Phase separation by low complexity domains promotes stress granule
887 assembly and drives pathological fibrillization. *Cell* **163**, 123-133 (2015).

888 43. Alberti, S., Gladfelter, A. & Mittag, T. Considerations and Challenges in Studying Liquid-
889 Liquid Phase Separation and Biomolecular Condensates. *Cell* **176**, 419-434 (2019).

890 44. Kubala, M.H., Kovtun, O., Alexandrov, K. & Collins, B.M. Structural and thermodynamic
891 analysis of the GFP:GFP-nanobody complex. *Protein Sci* **19**, 2389-2401 (2010).

892 45. Rothberg, K.G. *et al.* Caveolin, a protein component of caveolae membrane coats. *Cell* **68**,
893 673-682 (1992).

894 46. Shaul, P.W. & Anderson, R.G. Role of plasmalemmal caveolae in signal transduction. *Am J*
895 *Physiol* **275**, L843-851 (1998).

896 47. Ludwig, A. *et al.* Molecular composition and ultrastructure of the caveolar coat complex.
897 *PLoS Biol* **11**, e1001640 (2013).

898 48. Ludwig, A., Nichols, B.J. & Sandin, S. Architecture of the caveolar coat complex. *J Cell Sci*
899 **129**, 3077-3083 (2016).

900 49. Stoeber, M. *et al.* Model for the architecture of caveolae based on a flexible, net-like assembly
901 of Cavin1 and Caveolin discs. *Proc Natl Acad Sci U S A* **113**, E8069-E8078 (2016).

902 50. Snead, W.T. *et al.* BAR scaffolds drive membrane fission by crowding disordered domains.
903 *The Journal of cell biology* **218**, 664-682 (2019).

904 51. Wang, S., Zhao, Z. & Rodal, A.A. Higher-order assembly of Sorting Nexin 16 controls
905 tubulation and distribution of neuronal endosomes. *The Journal of cell biology* **218**, 2600
906 (2019).

907 52. Khater, I.M., Meng, F., Wong, T.H., Nabi, I.R. & Hamarneh, G. Super Resolution Network
908 Analysis Defines the Molecular Architecture of Caveolae and Caveolin-1 Scaffolds. *Scientific*
909 *Reports* **8**, 9009 (2018).

910 53. Liu, L. & Pilch, P.F. A critical role of cavin (polymerase I and transcript release factor) in
911 caveolae formation and organization. *J Biol Chem* **283**, 4314-4322 (2008).

912 54. Ariotti, N. *et al.* Modular Detection of GFP-Labeled Proteins for Rapid Screening by Electron
913 Microscopy in Cells and Organisms. *Developmental cell* **35**, 513-525 (2015).

914 55. Hetmanski, J.H.R. *et al.* Membrane Tension Orchestrates Rear Retraction in Matrix-Directed
915 Cell Migration. *Developmental cell* (2019).

916 56. Pelkmans, L. & Zerial, M. Kinase-regulated quantal assemblies and kiss-and-run recycling of
917 caveolae. *Nature* **436**, 128 (2005).

918 57. Siahaan, V. *et al.* Kinetically distinct phases of tau on microtubules regulate kinesin motors
919 and severing enzymes. *Nat Cell Biol* **21**, 1086-1092 (2019).

920 58. Tan, R. *et al.* Microtubules gate tau condensation to spatially regulate microtubule functions.
921 *Nat Cell Biol* **21**, 1078-1085 (2019).

922 59. Drechsler, H., Xu, Y., Geyer, V.F., Zhang, Y. & Diez, S. Multivalent electrostatic
923 microtubule-interactions of synthetic peptides are sufficient to mimic advanced MAP-like
924 behaviour. *Mol Biol Cell*, mbcE19050247 (2019).

925 60. Das, S., Eisen, A., Lin, Y.-H. & Chan, H.S. A Lattice Model of Charge-Pattern-Dependent
926 Polyampholyte Phase Separation. *The Journal of Physical Chemistry B* **122**, 5418-5431
927 (2018).

928 61. Borgia, A. *et al.* Extreme disorder in an ultrahigh-affinity protein complex. *Nature* **555**, 61-
929 66 (2018).

930 62. Lin, Y.-H., Forman-Kay, J.D. & Chan, H.S. Sequence-Specific Polyampholyte Phase
931 Separation in Membraneless Organelles. *Physical Review Letters* **117**, 178101 (2016).

932 63. Lin, Y.-H., Forman-Kay, J.D. & Chan, H.S. Theories for Sequence-Dependent Phase
933 Behaviors of Biomolecular Condensates. *Biochemistry* **57**, 2499-2508 (2018).

934 64. Feng, H., Zhou, B.R. & Bai, Y. Binding Affinity and Function of the Extremely Disordered
935 Protein Complex Containing Human Linker Histone H1.0 and Its Chaperone ProTalpha.
936 *Biochemistry* **57**, 6645-6648 (2018).

937 65. Pak, C.W. *et al.* Sequence Determinants of Intracellular Phase Separation by Complex
938 Coacervation of a Disordered Protein. *Mol Cell* **63**, 72-85 (2016).

939 66. Zeno, W.F. *et al.* Synergy between intrinsically disordered domains and structured proteins
940 amplifies membrane curvature sensing. *Nat Commun* **9**, 4152 (2018).

941 67. Zeno, W.F. *et al.* Molecular Mechanisms of Membrane Curvature Sensing by a Disordered
942 Protein. *J Am Chem Soc* **141**, 10361-10371 (2019).

943 68. Busch, D.J. *et al.* Intrinsically disordered proteins drive membrane curvature. *Nature*
944 *Communications* **6**, 7875 (2015).

945 69. Yoo, H., Triandafillou, C. & Drummond, D.A. Cellular sensing by phase separation: Using
946 the process, not just the products. *J Biol Chem* **294**, 7151-7159 (2019).

947 70. Aoki, T., Hagiwara, H., Matsuzaki, T., Suzuki, T. & Takata, K. Internalization of caveolae
948 and their relationship with endosomes in cultured human and mouse endothelial cells. *Anat*
949 *Sci Int* **82**, 82-97 (2007).

950 71. Boucrot, E., Howes, M.T., Kirchhausen, T. & Parton, R.G. Redistribution of caveolae during
951 mitosis. *J Cell Sci* **124**, 1965-1972 (2011).

952 72. Hayer, A. *et al.* Caveolin-1 is ubiquitinated and targeted to intralumenal vesicles in
953 endolysosomes for degradation. *The Journal of cell biology* **191**, 615-629 (2010).

954 73. Jung, W. *et al.* Cell-free formation and interactome analysis of caveolae. *The Journal of cell*
955 *biology* **217**, 2141-2165 (2018).

956 74. Pelkmans, L., Burli, T., Zerial, M. & Helenius, A. Caveolin-stabilized membrane domains as
957 multifunctional transport and sorting devices in endocytic membrane traffic. *Cell* **118**, 767-
958 780 (2004).

959 75. Shvets, E., Bitsikas, V., Howard, G., Hansen, C.G. & Nichols, B.J. Dynamic caveolae exclude
960 bulk membrane proteins and are required for sorting of excess glycosphingolipids. *Nat*
961 *Commun* **6**, 6867 (2015).

962 76. Murray, D.H. *et al.* An endosomal tether undergoes an entropic collapse to bring vesicles
963 together. *Nature* **537**, 107-111 (2016).

964 77. Miskei, M. *et al.* Fuzziness enables context dependence of protein interactions. *FEBS Lett*
965 **591**, 2682-2695 (2017).

966 78. Olsen, J.G., Teilum, K. & Kragelund, B.B. Behaviour of intrinsically disordered proteins in
967 protein-protein complexes with an emphasis on fuzziness. *Cell Mol Life Sci* **74**, 3175-3183
968 (2017).

969 79. Tompa, P. & Fuxreiter, M. Fuzzy complexes: polymorphism and structural disorder in
970 protein-protein interactions. *Trends Biochem Sci* **33**, 2-8 (2008).

971 80. Richter, T. *et al.* High-resolution 3D quantitative analysis of caveolar ultrastructure and
972 caveola-cytoskeleton interactions. *Traffic* **9**, 893-909 (2008).

973 81. McSwiggen, D.T., Mir, M., Darzacq, X. & Tjian, R. Evaluating phase separation in live cells:
974 diagnosis, caveats, and functional consequences. *Genes Dev* (2019).

975 82. Catanzariti, A.M., Soboleva, T.A., Jans, D.A., Board, P.G. & Baker, R.T. An efficient system
976 for high - level expression and easy purification of authentic recombinant proteins. *Protein*
977 *Science* **13**, 1331-1339 (2004).

978 83. Berrow, N.S. *et al.* A versatile ligation-independent cloning method suitable for high-
979 throughput expression screening applications. *Nucleic Acids Research* **35**, e45-e45 (2007).

980 84. Aboulaich, N., Vainonen, J.P., Stralfors, P. & Vener, A.V. Vectorial proteomics reveal
981 targeting, phosphorylation and specific fragmentation of polymerase I and transcript release
982 factor (PTRF) at the surface of caveolae in human adipocytes. *The Biochemical journal* **383**,
983 237-248 (2004).

85. Angelova, M.I. & Dimitrov, D.S. Liposome electroformation. *Faraday Discussions of the Chemical Society* **81**, 303-311 (1986).

86. Emsley, P. & Cowtan, K. Coot: model-building tools for molecular graphics. *Acta Crystallogr D Biol Crystallogr* **60**, 2126-2132 (2004).

87. Adams, P.D. *et al.* PHENIX: a comprehensive Python-based system for macromolecular structure solution. *Acta Crystallogr D Biol Crystallogr* **66**, 213-221 (2010).

993 **Figure Legends**

994 **Figure 1. The Cavin1 N- and C-terminal DR domains are important for self-association into**
995 **oligomers.**

996 **(A)** Schematic representation of Cavin1 and truncations. DR, disordered region; HR, helical region.
997 **(B)** The diffusion rate of Cavin1, Cavin1-ΔDR1 and Cavin1-ΔDR3 in solution assessed by
998 fluorescence correlation spectroscopy (FCS). Bacterially expressed and purified ubiquitin and GFP
999 tagged proteins (**Fig. S2**) were analysed in high NaCl concentration (500 mM) and physiological
1000 NaCl concentration (150 mM). Error bars indicate mean ± SD (standard deviation), N=2, n=10-15,
1001 ns – not significant, *P<0.05 ***P<0.001. **(C)** The diffusion rate of GFP-tagged Cavin1, Cavin1-
1002 ΔDR1 and Cavin1-ΔDR3 in lysates after expression in MCF7 cells (lacking endogenous Cavins and
1003 Caveolins). Buffer contained 150 mM NaCl. N=3, n=20-25, ns – not significant, ***P<0.001. Error
1004 bars indicate mean ± SD.

1005

1006 **Figure 2. Cavin1 undergoes liquid-liquid phase separation *in vitro*.**

1007 **(A)** Liquid-liquid phase separation (LLPS) assays with recombinant Ub- and GFP-tagged Cavin1,
1008 Cavin1-ΔDR3 and Cavin1-ΔDR1 at different protein and salt concentrations. Scale bar = 10 µm. **(B)**
1009 Fluorescence recovery after photobleaching (FRAP) assay with Cavin1, Cavin1-ΔDR3 and Cavin1-
1010 ΔDR1 showing GFP fluorescence images at increasing times. Scale bar = 5 µm**.** **(C)** Plot of
1011 normalized fluorescence intensity after photobleaching. N=6-8, Grey, blue and pink shaded areas
1012 around recovery curves represent standard deviation (SD). While Cavin1 and Cavin1-ΔDR3 droplets
1013 rapidly exchange with the bulk solution and recover their fluorescence, Cavin1-ΔDR1 shows virtually
1014 no exchange indicating gel formation.

1015

1016 **Figure 3. CAV1 N-terminus co-phase separates with cavin1**

1017 (**A**) Schematic representation of CAV1 domain architecture and design of various domain / point
1018 mutations. LLPS assays with MBP-GBP-CAV1 and cavin1 independently (**B**) and in mixture (**C**).
1019 MBP-GBP-CAV1 does not undergo LLPS in isolation but co-phase separates with Cavin1. (**D**) LLPS
1020 assays with different CAV1 DR region mutations and GFP-Cavin1 or Cavin1-DDR3 or Cavin1-
1021 DDR1. Scale bar – 10 µm. Among all domain mutations tested, only mCherry-CAV1 (1-100) was
1022 able to co-phase separate with cavin1. The charge inversion mutant M3 failed to co-phase separate
1023 highlighting the importance of charged residues in CAV1-cavin1 association.

1024

1025 **Figure 4. The Cavin1 DR domains are required for membrane remodelling *in vitro.***

1026 **(A)** Purified Ub-tagged full length Cavin1 was mixed with Folch 400 nm unilamellar liposomes and
1027 analysed by both negative stain EM (1% uranyl acetate) and cryoEM. (**B**) Cryoelectron tomography

1028 (CryoET) of Cavin1-coated membrane tubules showing bottom, middle and top sections of three-
1029 dimensional projections. Striated protein densities are observed coating the relatively heterogeneous
1030 membrane tubules. The full tomogram is shown in **Movie S1**. (**C**) Schematic diagram of Cavin1 and
1031 different truncation constructs examined for their ability to remodel membranes *in vitro*. **(D)** Purified
1032 Ub-tagged Cavin1 truncations were mixed with Folch 400 nm unilamellar liposomes and analysed
1033 by negative stain EM (1% uranyl acetate). Full membrane tubulation and remodelling activity
1034 requires residues 1-30 in DR1, and residues 330-345 in DR3. Scale bar = 500 nm.
1035
1036 **Figure 5. Removing the Cavin1 DR domains prevents deformation of GUV membranes.**
1037 **(A)** Purified Ub- and GFP-tagged Cavin1 shows strong localised clustering on the surface of Folch
1038 giant multilamellar vesicles (GMV) containing Bodipy-TMR-labelled PI(4,5)P_2 (0.1 mol%). Cavin1
1039 **(B)**, Cavin1-ΔDR3 **(C)** or Cavin1-ΔDR1 **(D)** were incubated with Folch GMVs containing Bodipy-
1040 TMR-labelled PI(4,5)P_2 (0.1 mol%), allowed to settle on glass coverslips and images were acquired
1041 one frame per second. **(E)** GUVs incubated with Cavin1-ΔDR1 were often observed to be tethered to
1042 each other with Cavin1-ΔDR1 concentrated at the contact sites. Scale bar = 10 µm.
1043
1044 **Figure 6. The Cavin1 DR domains are essential for caveola formation with CAV1.**
1045 (**A**) GFP-tagged Cavin1 and truncations (green) were expressed for 24 h in PC3 cells, fixed and
1046 immunolabelled for Caveolin1 (CAV1) (red). Full length Cavin1 forms typical caveola puncta,
1047 colocalising with CAV1 at the cell surface. Cavin1-ΔDR1 mutant expression leads to formation of
1048 tethered intracellular CAV1-positive clusters. Cavin1-ΔDR3 shows cytoplasmic and microtubule
1049 localisation. Images were collected using a Zeiss fast Airyscan microscope. Scale bar = 10 µm.
1050 Fluorescence recovery after photobleaching (FRAP) analysis of GFP-Cavin1-ΔDR3 before **(B)** and
1051 after **(C)** nocodazole (10 µM) addition**.** Scale bar – 5 µm **(D)** In PC3 cells GFP-tagged Cavin1-ΔDR1
1052 truncation shows colocalization with the early endosomal marker (EEA1) (red) and CAV1 (blue).
1053 Inset shows merge images of GFP-Cavin1-ΔDR1/EEA1 and GFP-Cavin1-ΔDR1/CAV1. Scale bar =
1054 10 µm. (**E**) GFP-tagged Cavin1 and Cavin1-ΔDR1 were visualised in PC3 cells by electron
1055 microscopy and labelling of GFP tagged proteins using APEX-GBP staining. Scale bar = 1 µm.**(F)**
1056 Live imaging of PC3 cells expressing Rab5a-mCherry with either GFP-Cavin1 or GFP-Cavin1-
1057 ΔDR1. Images were acquired one frame per four seconds and frame numbers are indicated in boxes.
1058 Arrows indicate mCherry/GFP signal co-localisation or separation event.
1059
1060 **Figure 7. Definition of the minimal DR sequences required for Cavin1 function.**

1061 **(A)** GFP-tagged Cavin1 DR domain truncation mutants (green) (**Fig. 4C**) were expressed in PC3 cells
1062 and immunolabelled with CAV1 (red). Residues 1-30 in DR1 and 330-345 are required for caveola
1063 formation. Scale bar = 10 µm. (**B**) APEX-GBP labelling of GFP tagged Cavin1(1-345) shows normal
1064 bulb-shaped caveolae at the plasma membrane. **(C)** Proximity ligation assay (PLA) analyses show
1065 that truncation of Cavin1 from the C-terminus beyond residue 345 results in loss of association with
1066 CAV1. PLA signal was quantified as dots per cell for specific interaction between GFP-tagged
1067 proteins and CAV1, N = 2 (independent biological replicates), n = 10-15 (cells per replicates), Error
1068 bars indicate mean ± SD, *** P<0.001.
1069
1070 **Figure 8. Sequence requirements of the Cavin1 DR domains in caveola assembly.**
1071 **(A)** Schematic diagram of Cavin1(1-345) with the sequences of the various point mutants indicated.
1072 DR1, DR2 and DR3 mutations occur in the regions 1-30, 161-197 and 311-345 respectively. **(B)**
1073 GFP-tagged Cavin1(1-345) DR1 domain mutants (green), (**C**) DR2 domain mutants and (**D**) DR3
1074 domain mutants expressed in PC3 cells and immunolabelled with endogenous CAV1 (red). Images
1075 in (B), (C) and (D) were by Airyscan confocal microscopy. Scale bar = 10 µm. **(E)** FRAP analysis of
1076 Cavin1 (1-345) DR3mut9 mutant showing fast recovery of fluorescence in cytosolic droplets and also
1077 droplet fusion events (marked by arrow).
1078
1079 **Figure 9. Model for the role of Cavin1 DR domains in LLPS and caveola formation.**
1080 **(A)** Structural model of a Cavin1 homotrimeric assembly. The trimeric HR1 coiled-coil domain is
1081 derived from the crystal structure of the mouse Cavin1 HR1 domain [11], the UC1 and HR2 domains
1082 are modelled as described previously [10], and the DR domains are modelled as random coil structures
1083 (see Methods for further details). The structure is shown in ribbon diagram (top) and with an
1084 electrostatic surface representation (bottom). **(B)** Proposed orientation of Cavin1 proteins on the
1085 membrane surface, with membrane-binding HR1 and HR2 domains associated with the phospholipid
1086 bilayer and negatively-charged DR sequences directed outwards due to electrostatic repulsion. (**C**)
1087 Potential role of Cavin1 disordered sequences in membrane curvature generation due to steric
1088 crowding. This concept is largely derived from previous studies of other membrane-associated
1089 proteins [66, 67]. (**D**) Potential role of Cavin1 fuzzy interactions and LLPS in membrane curvature
1090 generation, CAV1 interaction and caveola formation.
1091
1092

1093 **Supplementary Information**

1094 **Figure S1. Electrostatic charge distribution and sequence disorder in the Cavin family proteins.**
1095 **(A)** Protein charge plots of human (h) and zebrafish (z) cavin family proteins performed using the
1096 Emboss Server (http://www.bioinformatics.nl/cgi-bin/emboss/charge) (using standard input
1097 parameters and a window width of five amino acid residues). **(B)** The Cavin1 sequence was analysed
1098 using the D2P2 web server [15] for predicted regions of disorder, and also known sites of post-
1099 translational modifications.

1100

1101 **Figure S2. Schematic representation of protein expression constructs used in this study.**

1102

1103 **Figure S3. LLPS behaviour of recombinant Cavin1 expressed in bacteria**
1104 (**A**) Liquid-liquid phase separation (LLPS) assay with bacterially expressed recombinant Ub- and
1105 GFP-tagged Cavin1, at different protein and salt concentrations but in the absence of dextran or other
1106 crowding agents. (**B**) At low concentrations, full length Cavin1 still forms liquid droplets, and
1107 Cavin1-ΔDR1 still forms coacervates. Cavin1-ΔDR3 is less prone to LLPS at low concentrations
1108 compared to the full-length protein. (**C**) LLPS assay performed with GFP tagged Cavin1-ΔDR1 by
1109 addition of 1.25% dextran T-500. Fluorescent GFP signal and adjacent bright filed image showing
1110 transparent drops unlike non-specific precipitates that are usually non-transparent and milky or brown
1111 in appearance. Scale bar – 10 µm.

1112

1113 **Figure S4. Cavin1 undergoes LLPS and remodels cellular membranes devoid of CAV1.**
1114 (**A**) LLPS assay performed with Cavin1-GFP expressed and purified from mammalian HEK293 cells.
1115 (**B**) MCF7 cell lysates expressing Cavin1-GFP with the addition of 3% dextran T-500 in either 150
1116 mM NaCl or 500 mM NaCl. Scale bar – 10 µm. (**C**) MCF7 cells expressing GFP-Cavin1, Cavin1-
1117 ΔDR1 showing cytosolic distribution and Cavin1-ΔDR3 showing diffuse localisation (upper panel).
1118 Addition of a water-soluble form of cholesterol (1 mM added, with effective available cholesterol
1119 concentration ~40 µM) to cells expressing GFP-Cavin1 promotes liquid like droplet formation,
1120 membrane recruitment, and in some cells and tubulation in some cells (lower panels). Scale bar – 10
1121 µm. (**D**) CAV1$^{-/-}$ MEF cells expressing GFP-Cavin1 show cytosolic distribution and addition of 1
1122 mM cholesterol causes membrane recruitment of GFP-Cavin1 (left panels) also observed by
1123 ruthenium red labelling of membrane surface by EM. Scale bar – 1 µm.

1124

1125 **Figure S5. Co-phase separation of CAV1 with Cavin1.**

1126 **(A)** In gel fluorescence images of gel filtration fractions for respective mCherry-tagged CAV1
1127 mutants. **(B)** LLPS assay with mCherry CAV1 (1-30), (30-80), (1-80) and (1-100) and Cavin1.
1128 mCherry-CAV1 (1-100) is recruited to cavin1 droplets and undergo LLPS.
1129
1130 **Figure S6. Cavin1 membrane interactions *in vitro***
1131 **(A)** *In vitro* membrane tubulation assay and negative stain electron microscopy was performed after
1132 mixing Cavin1 and liposomes consisting of Phosphatidylcholine (PC) and Phosphatidylethanolamine
1133 (PE) or PC/PE liposomes containing PI(4,5)P_2 and Phosphatidylserine (PS) or Folch liposomes
1134 containing 0.1 mol% TMR labelled PI(4,5)P_2 to replicate conditions in **Figure 5**. (**B**) In vitro
1135 membrane tubulation assay performed by mixing mammalian Cavin1-GFP with Folch liposomes,
1136 with membrane tubules highlighted in insets. Scale bar – 1 µm. **(C)** Dose dependent GFP-Cavin1
1137 interaction with GUVs containing rhodamine-PE or Bodipy-TMR-PI(4,5)P_2.
1138
1139 **Figure S7. Localisation of Cavin1 with truncated DR1 and DR3 domains.**
1140 **(A)** Confocal microscopy images of GFP-Cavin1, GFP-Cavin1-ΔDR1 and GFP-Cavin1-ΔDR3
1141 immunolabelled with CAV1 (red) **(B)** GFP-Cavin1-ΔDR3 (green) associates with microtubules (red)
1142 in PC3 cells and disperses to the cytosol and forms liquid droplets after nocodazole treatment.
1143 Fluorescence images acquired with a Zeiss Airyscan2 microscope. (**C**) Cavin1-ΔDR1-GFP with a C-
1144 terminal GFP tag shows a similar intracellular accumulation with CAV1 in PC3 cells as the N-
1145 terminal GFP-tagged protein (**Fig. 6A**), suggesting that the GFP tag does not contribute to this
1146 phenotype.
1147
1148 **Figure S8. Comparison of Cavin1 truncation mutants with endocytic markers.**
1149 **(A)** GFP-tagged Cavin1-ΔDR1 (green) was expressed in PC3 cells, and fixed cells were
1150 immunolabelled for CAV1 (blue) and different endocytic markers (red) including EEA1, GM130,
1151 LAMP1 and Rab11. Only EEA1 showed significant overlap with the internalised Cavin1-ΔDR1 and
1152 CAV1 positive structures. **(B)** High-resolution images of GFP-tagged Cavin1 and Cavin1-ΔDR1
1153 (green) in PC3 cells compared with EEA1 (magenta) acquired with a Zeiss Airyscan2 microscope.
1154 (**C**) As for (**A**) but cells expressing GFP-tagged Cavin1(30-392). Cavin1(30-392) accumulates at
1155 intracellular structures with CAV1 and positive for EEA1 labelling similarly to Cavin1-ΔDR1 with
1156 the full deletion of the DR1 domain.
1157
1158 **Figure S9. Cavin1-ΔDR1 shows colocalisation with internalised transferrin.**

1159 Transferrin uptake assay was performed in PC3 cells expressing either mCherry-tagged Cavin1 or
1160 Cavin1-ΔDR1 (red) with transferrin Alexa-488 (green). Wild-type mCherry-Cavin1 showed no
1161 colocalization with endocytosed transferrin whereas mCherry-Cavin1-ΔDR1 formed large structures
1162 (red) with transferrin positive endosomes surrounding them.
1163
1164 **Figure S10. PLA assay of Cavin1 interactions with CAV1**
1165 Representative images of proximity ligation assays of Cavin1 and CAV1 interactions, with GFP-
1166 tagged Cavin1 mutants in green and PLA signal in red. Scale bar – 10 µm. Related to **Fig. 7C.**
1167
1168 **Figure S11. Localisation and membrane remodelling by Cavin1(1-345) mutant proteins.**
1169 **(A)** GFP-tagged Cavin1(1-345) mutant DR1mut1 was expressed in PC3 cells, and fixed cells were
1170 immunolabelled for CAV1 (blue) and different endocytic markers (red) including EEA1, GM130,
1171 and LAMP1. Like the complete deletion of the residues 1-30 in the Cavin1 DR1 region (**Fig. S7C**)
1172 Cavin1(1-345) mutant DR1mut1 shows significant overlap with CAV1 and EEA1 positive internal
1173 structures. **(B)** APEX-GBP labelling of GFP-tagged Cavin1(1-345) mutant DR1mut1 shows
1174 accumulation and clustering with internal membrane vesicles (arrows). (**C**) The diffusion rate
1175 measured by FCS of selected GFP-tagged Cavin1(1-345) DR mutants in lysates after expression in
1176 MCF7 cells (lacking endogenous Cavins and Caveolins). N = 3, n = 15-25. Error bars indicate mean
1177 ± SD, **P<0.05, *** P<0.001, ns – not significant. (**D**) APEX-GBP labelling of GFP-tagged
1178 Cavin1(1-345) mutant DR3mut9 shows droplet localisation (arrows). (**E**) Purified Ub-tagged
1179 Cavin1(1-345) mutant DR3mut9 was mixed with unilamellar Folch liposomes (extruded to 400 nm
1180 diameter) and analysed by negative stain EM (1% uranyl acetate). This mutant is able to remodel and
1181 tubulate these synthetic membranes, although with a slightly larger diameter than wild-type Cavin or
1182 Cavin1(1-345) (**Fig. 4D**).
1183
1184 **Figure S12.** Gels showing purified recombinant Cavin1 proteins used in this study (**A to G**), and
1185 western blot (**H**) showing expression of GFP tagged mutants expressed in PC3 cell line probed with
1186 anti-GFP antibody. The diffusion time measurements for three dyes performed before session (**I**).
1187
1188

1189 **Movie S1. (related to Fig. 4B).**

1190 Cryoelectron tomography (CryoET) of Cavin1-coated membrane tubules. The movies shows a series
1191 of images panning through the three-dimensional tomographic volume. Striated protein densities are
1192 observed coating the relatively heterogeneous membrane tubules.

1193

1194 **Movie S2. (related to Fig. 6B).**

1195 GFP-tagged Cavin1-ΔDR3 was expressed in PC3 cells and photobleaching was performed on a small
1196 region along microtubules coated with GFP tagged mutant protein. Images were acquired one frame
1197 per second.

1198

1199 **Movie S3. (related to Fig. 6C).**

1200 GFP-tagged Cavin1-ΔDR3 was expressed in PC3 cells and treated with nocodazole (10 μM).
1201 Photobleaching was performed on a small region containing liquid droplets of mutant protein and
1202 images were acquired one frame per second.

1203

1204 **Movie S4. (related to Fig. 6F).**

1205 GFP-tagged Cavin1 and Rab5a-mCherry were co-expressed in PC3 cells and images were acquired
1206 one frame per four seconds.

1207

1208 **Movie S5. (related to Fig. 6F).**

1209 GFP-tagged Cavin1-ΔDR1 and Rab5a-mCherry were co-expressed in PC3 cells and images were
1210 acquired one frame per four seconds.

1211

1212 **Movie S6. (Related to Fig. 8E).**

1213 GFP-Cavin1 DR3mut9 mutant expressed in PC3 cell line and photobleaching was performed on
1214 protein droplets dispersed in cytosol. Images were acquired one frame per two seconds.

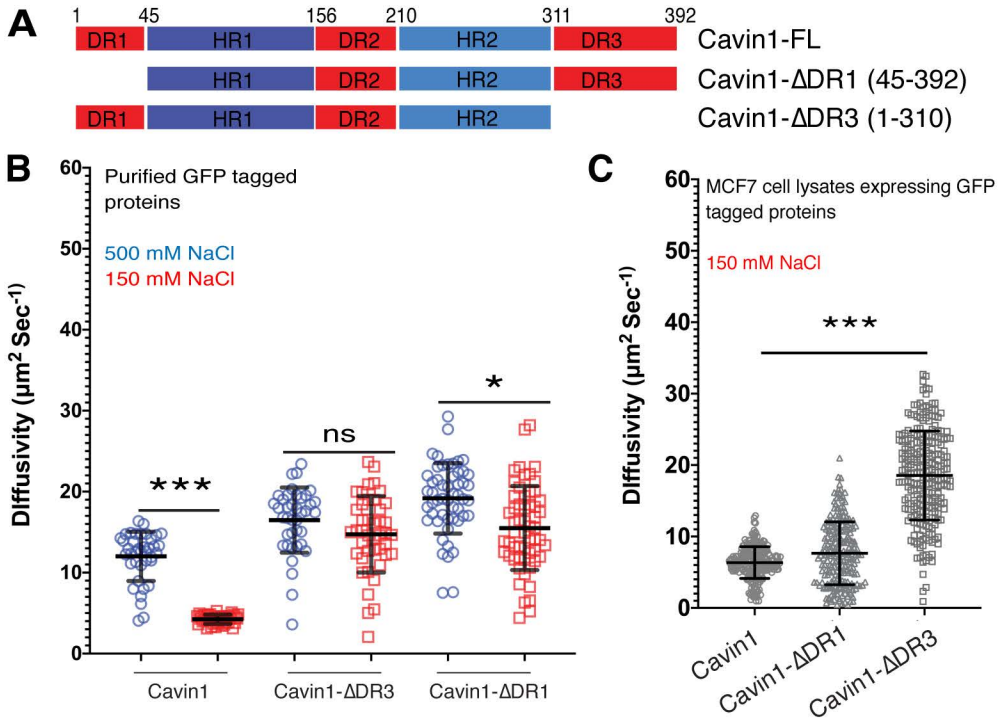

Figure 1. The Cavin1 N- and C-terminal DR domains are important for self-association into oligomers.
(A) Schematic representation of Cavin1 and truncations. DR, disordered region; HR, helical region. (B) The diffusion rate of Cavin1, Cavin1-ΔDR1 and Cavin1-ΔDR3 in solution assessed by fluorescence correlation spectroscopy (FCS). Bacterially expressed and purified ubiquitin and GFP tagged proteins (Fig. S2) were analysed in high NaCl concentration (500 mM) and physiological NaCl concentration (150 mM). Error bars indicate mean ± SD (standard deviation), N=2, n=10-15, ns – not significant, *P<0.05 ***P<0.001. (C) The diffusion rate of GFP-tagged Cavin1, Cavin1-ΔDR1 and Cavin1-ΔDR3 in lysates after expression in MCF7 cells (lacking endogenous Cavins and Caveolins). Buffer contained 150 mM NaCl. N=3, n=20-25, ns – not significant, ***P<0.001. Error bars indicate mean ± SD.

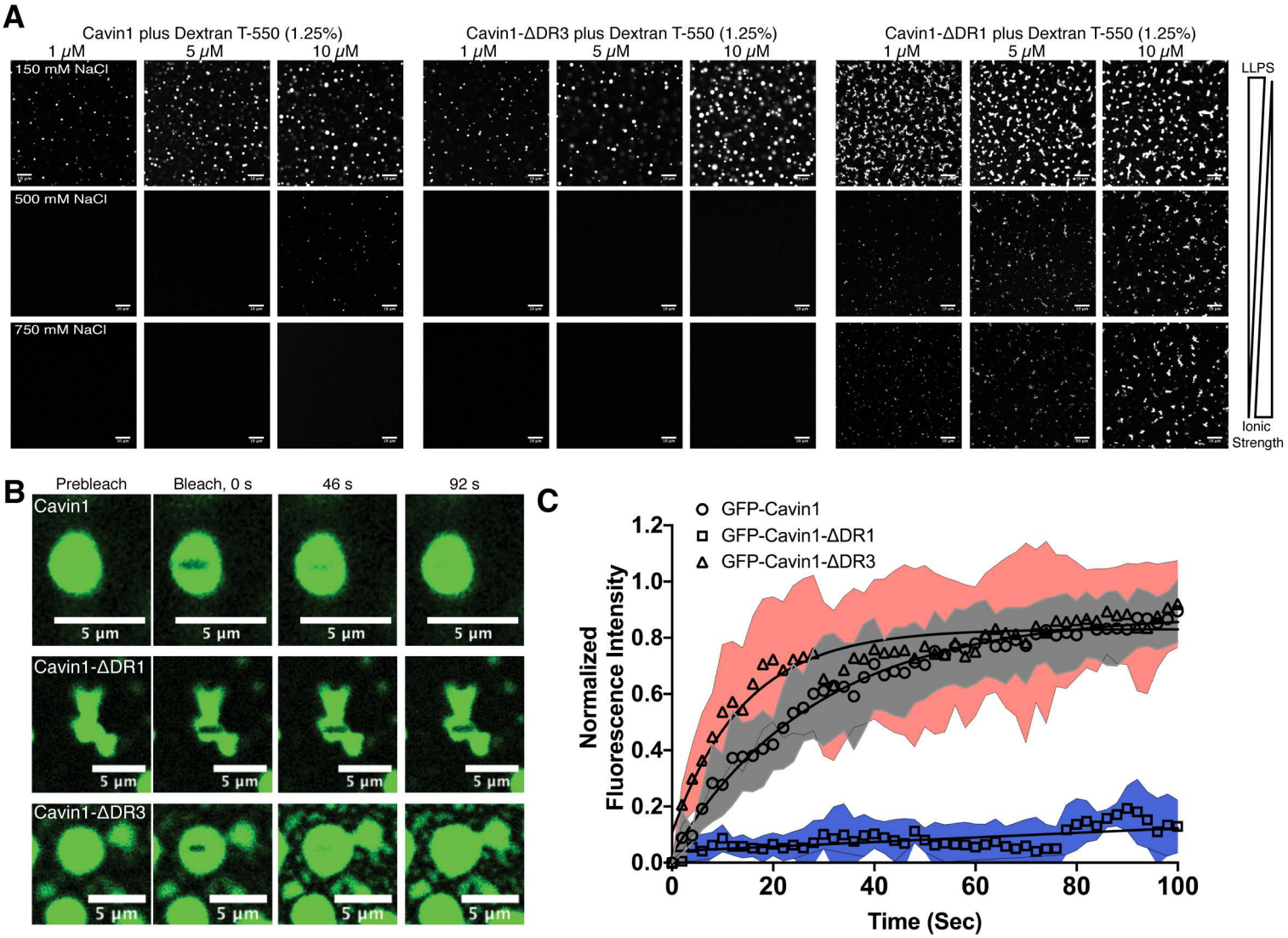

Figure 2. Cavin1 undergoes liquid-liquid phase separation in vitro.
(A) Liquid-liquid phase separation (LLPS) assays with recombinant Ub- and GFP-tagged Cavin1, Cavin1-ΔDR3 and Cavin1-ΔDR1 at different protein and salt concentrations. Scale bar = 10 µm. (B) Fluorescence recovery after photobleaching (FRAP) assay with Cavin1, Cavin1-ΔDR3 and Cavin1-ΔDR1 showing GFP fluorescence images at increasing times. Scale bar = 5 µm. (C) Plot of normalized fluorescence intensity after photobleaching. N=6-8, Grey, blue and pink shaded areas around recovery curves represent standard deviation (SD). While Cavin1 and Cavin1-ΔDR3 droplets rapidly exchange with the bulk solution and recover their fluorescence, Cavin1-ΔDR1 shows virtually no exchange indicating gel formation.

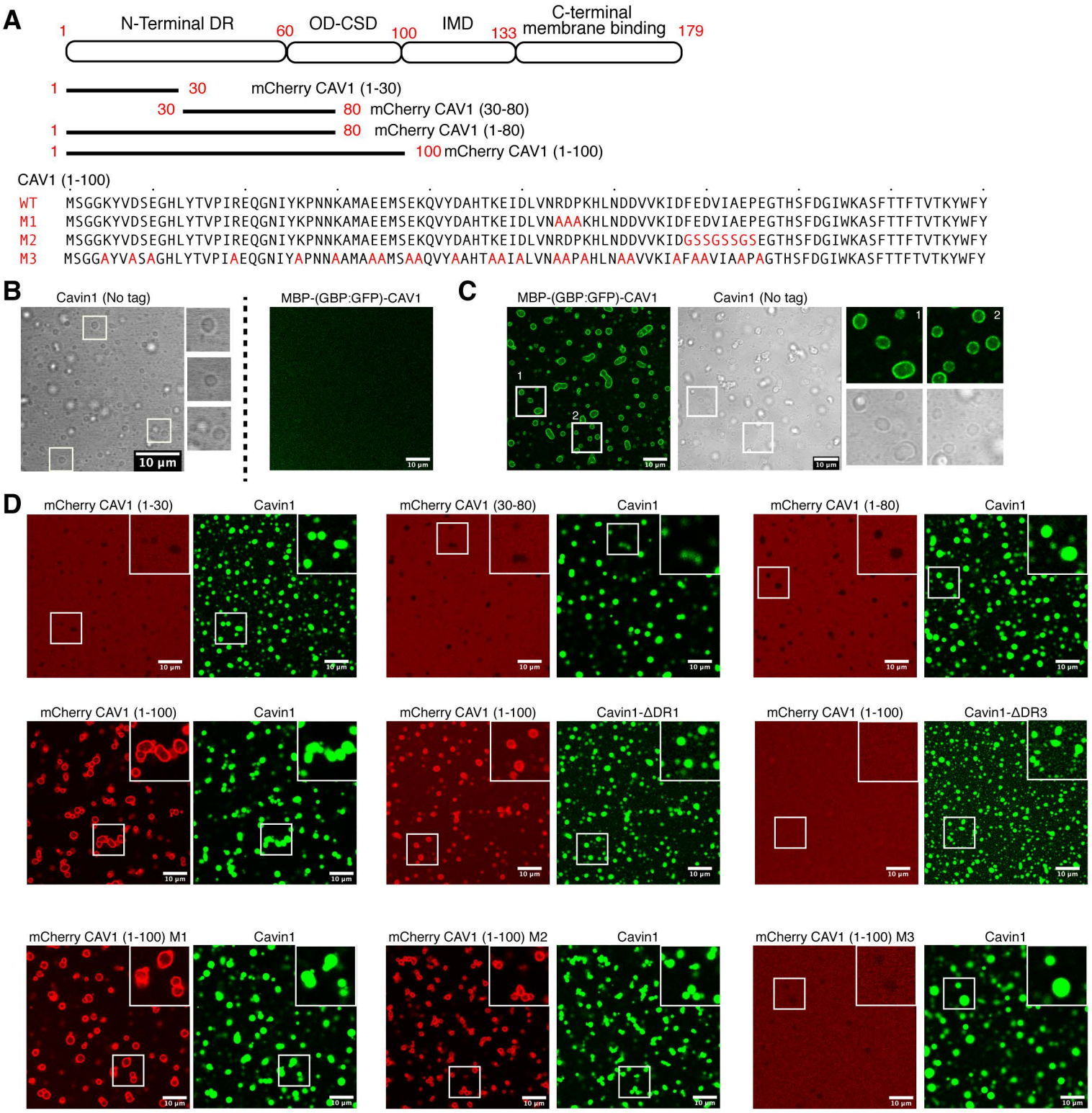

Figure 3. CAV1 N-terminus co-phase separates with cavin1

(A) Schematic representation of CAV1 domain architecture and design of various domain / point mutations. LLPS assays with MBP-GBP-CAV1 and cavin1 independently (B) and in mixture (C). MBP-GBP-CAV1 does not undergo LLPS in isolation but co-phase separates with Cavin1. (D) LLPS assays with different CAV1 DR region mutations and GFP-Cavin1 or Cavin1-ΔDR3 or Cavin1-ΔDR1. Scale bar – 10 µm. Among all domain mutations tested, only mCherry-CAV1 (1-100) was able to co-phase separate with cavin1. The charge inversion mutant M3 failed to co-phase separate highlighting the importance of charged residues in CAV1-cavin1 association.

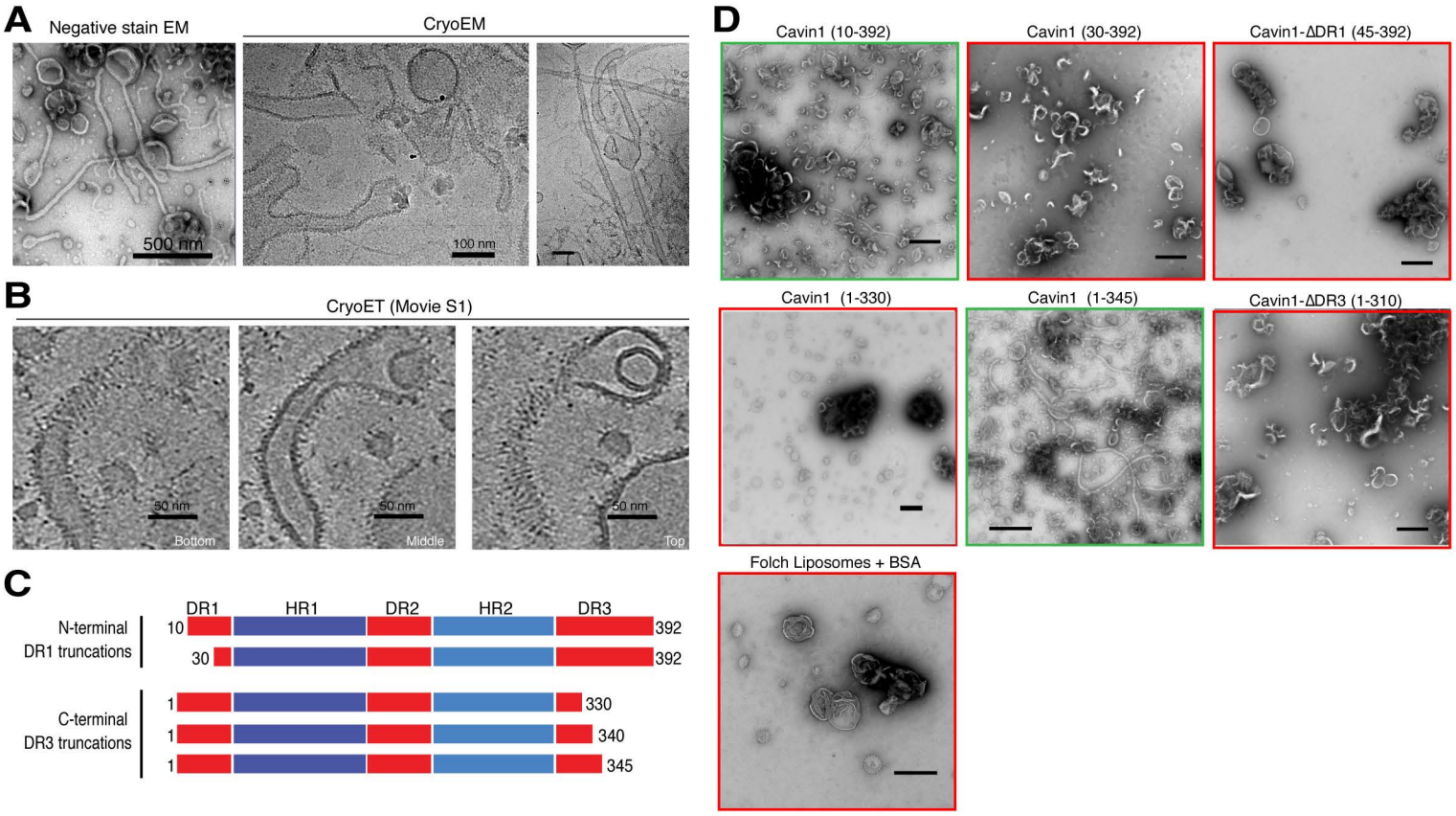

Figure 4. The Cavin1 DR domains are required for membrane remodelling in vitro.
(A) Purified Ub-tagged full length Cavin1 was mixed with Folch 400 nm unilamellar liposomes and analysed by both negative stain EM (1% uranyl acetate) and cryoEM. (B) Cryoelectron tomography (CryoET) of Cavin1-coated membrane tubules showing bottom, middle and top sections of three-dimensional projections. Striated protein densities are observed coating the relatively heterogeneous membrane tubules. The full tomogram is shown in Movie S1. (C) Schematic diagram of Cavin1 and different truncation constructs examined for their ability to remodel membranes in vitro. (D) Purified Ub-tagged Cavin1 truncations were mixed with Folch 400 nm unilamellar liposomes and analysed by negative stain EM (1% uranyl acetate). Full membrane tubulation and remodelling activity requires residues 1-30 in DR1, and residues 330-345 in DR3. Scale bar = 500 nm.

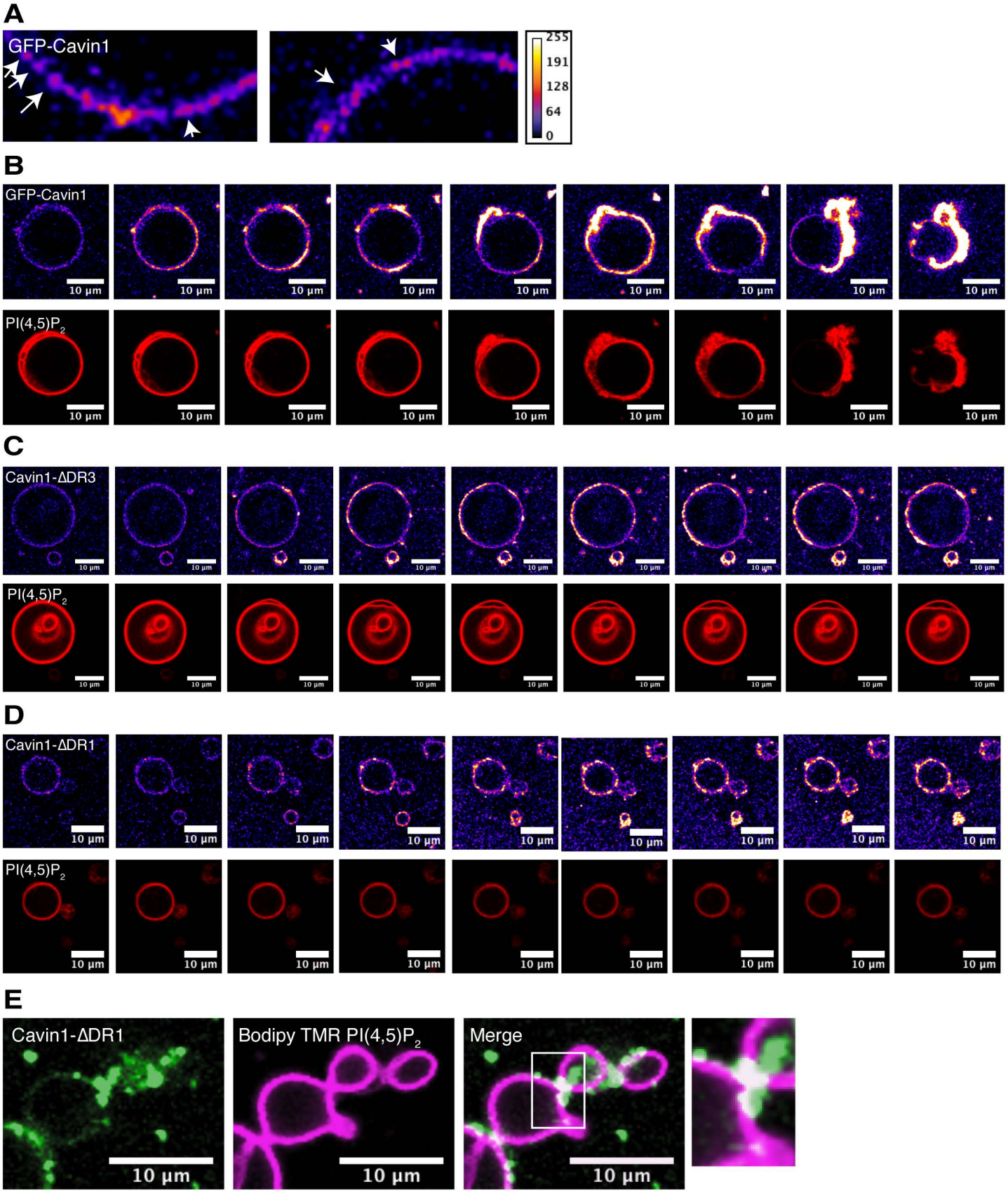

Figure 5. Removing the Cavin1 DR domains prevents deformation of GUV membranes.
(A) Purified Ub- and GFP-tagged Cavin1 shows strong localised clustering on the surface of Folch giant multilamellar vesicles (GMV) containing Bodipy-TMR-labelled PI(4,5)P2 (0.1 mol%). Cavin1 (B), Cavin1-ΔDR3 (C) or Cavin1-ΔDR1 (D) were incubated with Folch GMVs containing Bodipy-TMR-labelled PI(4,5)P2 (0.1 mol%), allowed to settle on glass coverslips and images were acquired one frame per second. (E) GUVs incubated with Cavin1-ΔDR1 were often observed to be tethered to each other with Cavin1-ΔDR1 concentrated at the contact sites. Scale bar = 10 µm.

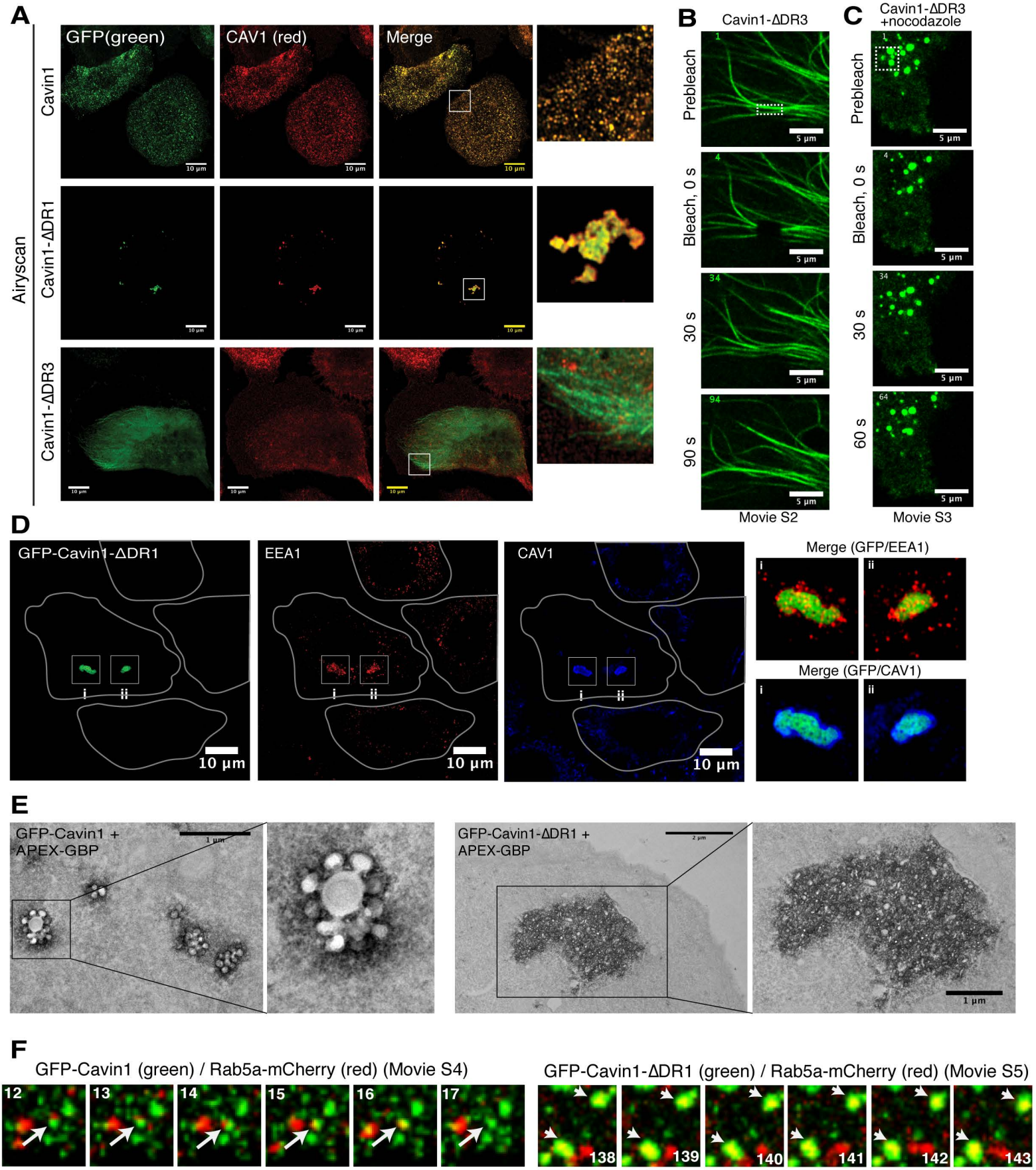

Figure 6. The Cavin1 DR domains are essential for caveola formation with CAV1.
(A) GFP-tagged Cavin1 and truncations (green) were expressed for 24 h in PC3 cells, fixed and immunolabelled for Caveolin1 (CAV1) (red). Full length Cavin1 forms typical caveola puncta, colocalising with CAV1 at the cell surface. Cavin1-ΔDR1 mutant expression leads to formation of tethered intracellular CAV1-positive clusters. Cavin1-ΔDR3 shows cytoplasmic and microtubule localisation. Images were collected using a Zeiss fast Airyscan microscope. Scale bar = 10 µm. Fluorescence recovery after photobleaching (FRAP) analysis of GFP-Cavin1-ΔDR3 before (B) and after (C) nocodazole (10 μM) addition. Scale bar – 5 µm (D) In PC3 cells GFP-tagged Cavin1-ΔDR1 truncation shows colocalization with the early endosomal marker (EEA1) (red) and CAV1 (blue). Inset shows merge images of GFP-Cavin1-ΔDR1/EEA1 and GFP-Cavin1-ΔDR1/CAV1. Scale bar = 10 µm. (E) GFP-tagged Cavin1 and Cavin1-ΔDR1 were visualised in PC3 cells by electron microscopy and labelling of GFP tagged proteins using APEX-GBP staining. Scale bar = 1 µm.(F) Live imaging of PC3 cells expressing Rab5a-mCherry with either GFP-Cavin1 or GFP-Cavin1-ΔDR1. Images were acquired one frame per four seconds and frame numbers are indicated in boxes. Arrows indicate mCherry/GFP signal co-localisation or separation event.

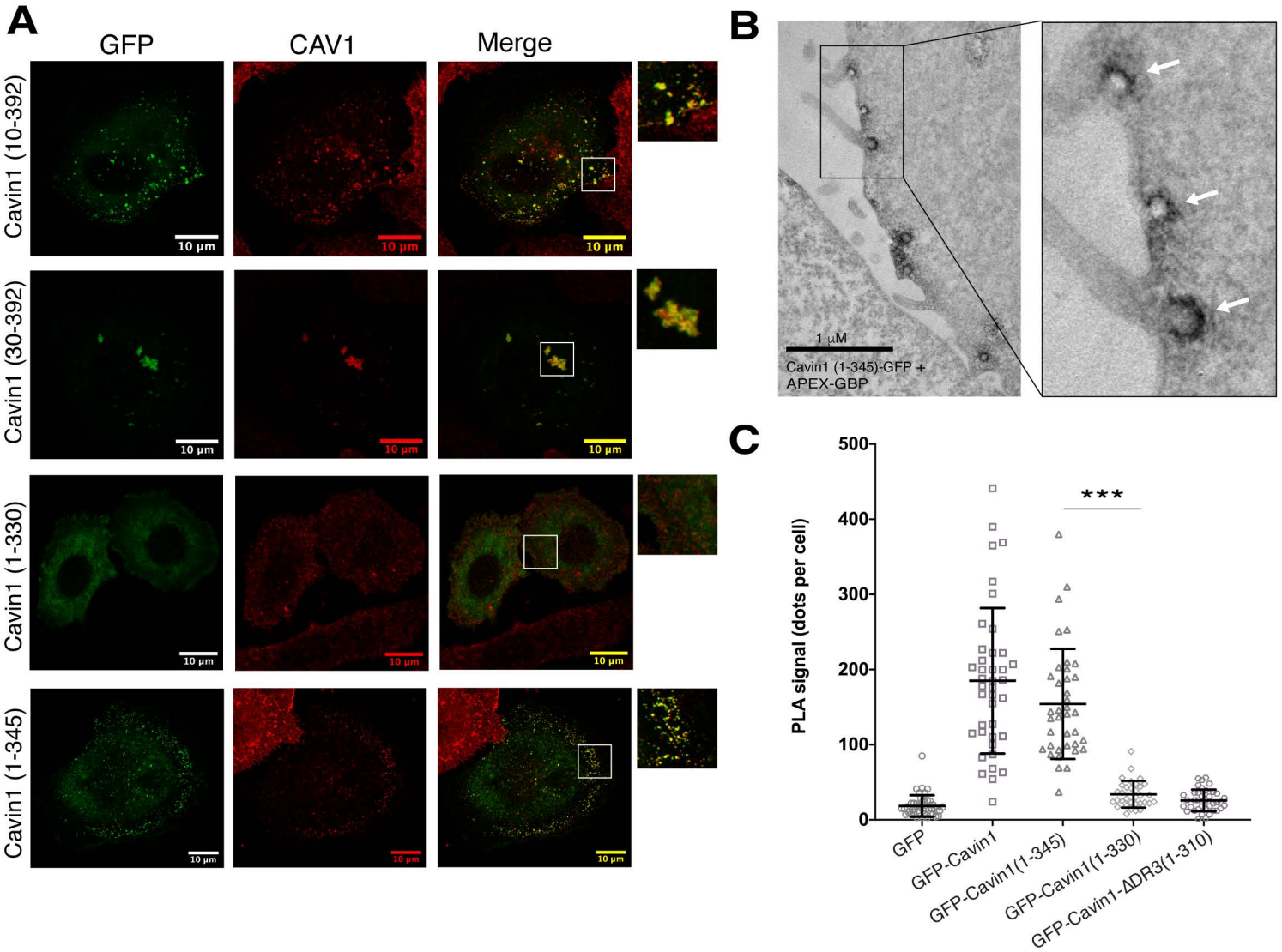

Figure 7. Definition of the minimal DR sequences required for Cavin1 function.
(A) GFP-tagged Cavin1 DR domain truncation mutants (green) (Fig. 3C) were expressed in PC3 cells and immunolabelled with CAV1 (red). Residues 1-30 in DR1 and 330-345 are required for caveola formation. Scale bar = 10 µm. (B) APEX-GBP labelling of GFP tagged Cavin1(1-345) shows normal bulb-shaped caveolae at the plasma membrane. (C) Proximity ligation assay (PLA) analyses show that truncation of Cavin1 from the C-terminus beyond residue 345 results in loss of association with CAV1. PLA signal was quantified as dots per cell for specific interaction between GFP-tagged proteins and CAV1, N = 2 (independent biological replicates), n = 10-15 (cells per replicates), Error bars indicate mean ± SD, *** P<0.001.

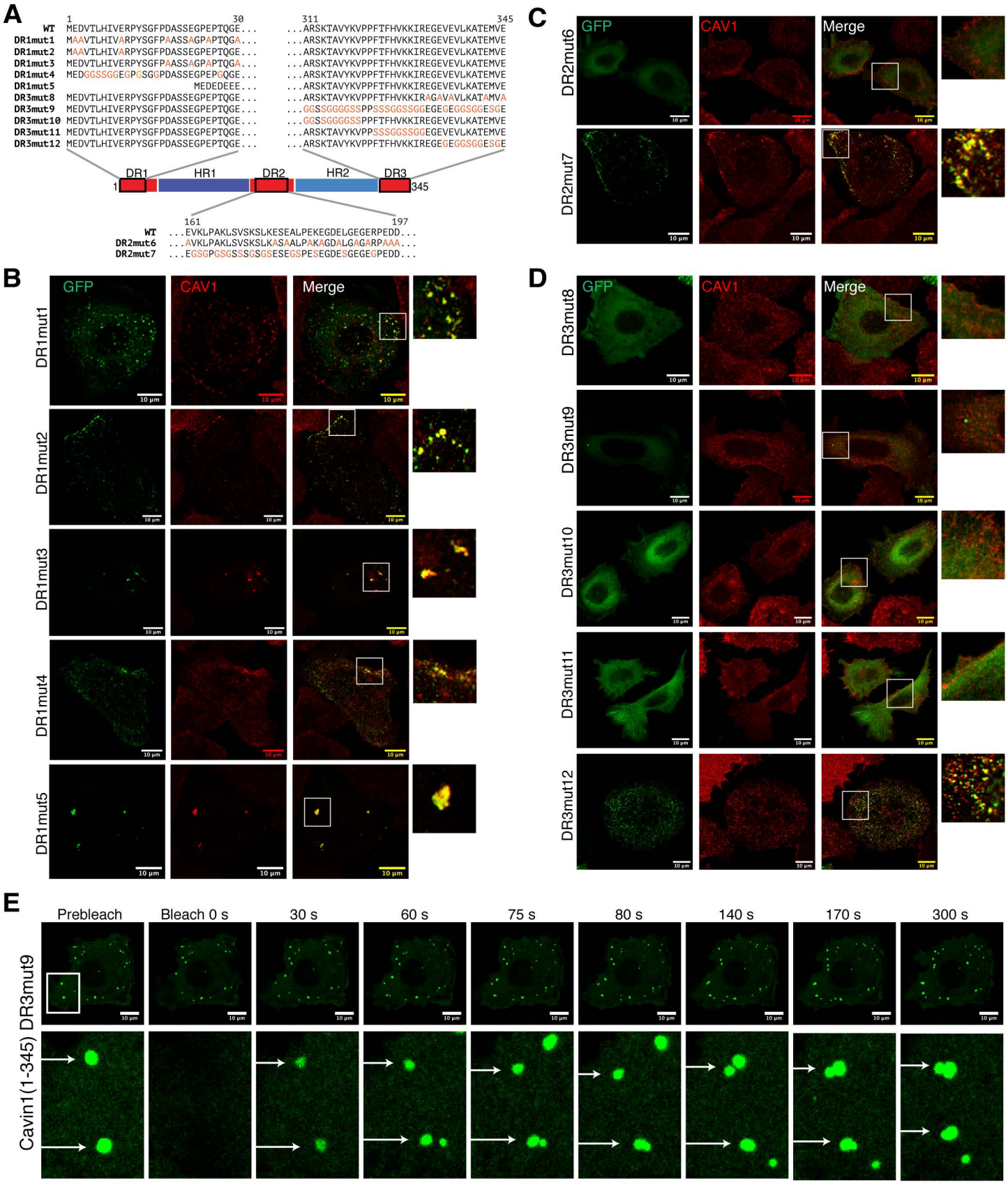

Figure 8. Sequence requirements of the Cavin1 DR domains in caveola assembly.
(A) Schematic diagram of Cavin1(1-345) with the sequences of the various point mutants indicated. DR1, DR2 and DR3 mutations occur in the regions 1-30, 161-197 and 311-345 respectively. (B) GFP-tagged Cavin1(1-345) DR1 domain mutants (green), (C) DR2 domain mutants and (D) DR3 domain mutants expressed in PC3 cells and immunolabelled with endogenous CAV1 (red). Images in (B), (C) and (D) were by Airyscan confocal microscopy. Scale bar = 10 μm. (E) FRAP analysis of Cavin1 (1-345) DR3mut9 mutant showing fast recovery of fluorescence in cytosolic droplets and also droplet fusion events (marked by arrow).

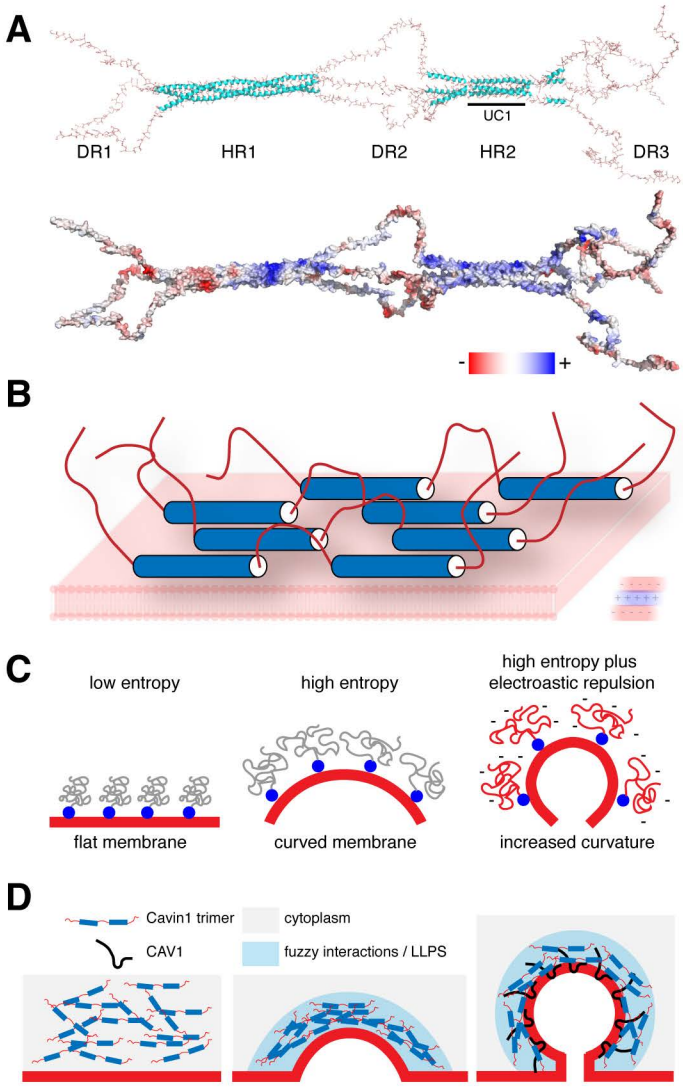

Figure 9. Model for the role of Cavin1 DR domains in LLPS and caveola formation.
(A) Structural model of a Cavin1 homotrimeric assembly. The trimeric HR1 coiled-coil domain is derived from the crystal structure of the mouse Cavin1 HR1 domain 11, the UC1 and HR2 domains are modelled as described previously 10, and the DR domains are modelled as random coil structures (see Methods for further details). The structure is shown in ribbon diagram (top) and with an electrostatic surface representation (bottom). (B) Proposed orientation of Cavin1 proteins on the membrane surface, with membrane-binding HR1 and HR2 domains associated with the phospholipid bilayer and negatively-charged DR sequences directed outwards due to electrostatic repulsion. (C) Potential role of Cavin1 disordered sequences in membrane curvature generation due to steric crowding. This concept is largely derived from previous studies of other membrane-associated proteins 65, 66. (D) Potential role of Cavin1 fuzzy interactions and LLPS in membrane curvature generation, CAV1 interaction and caveola formation.

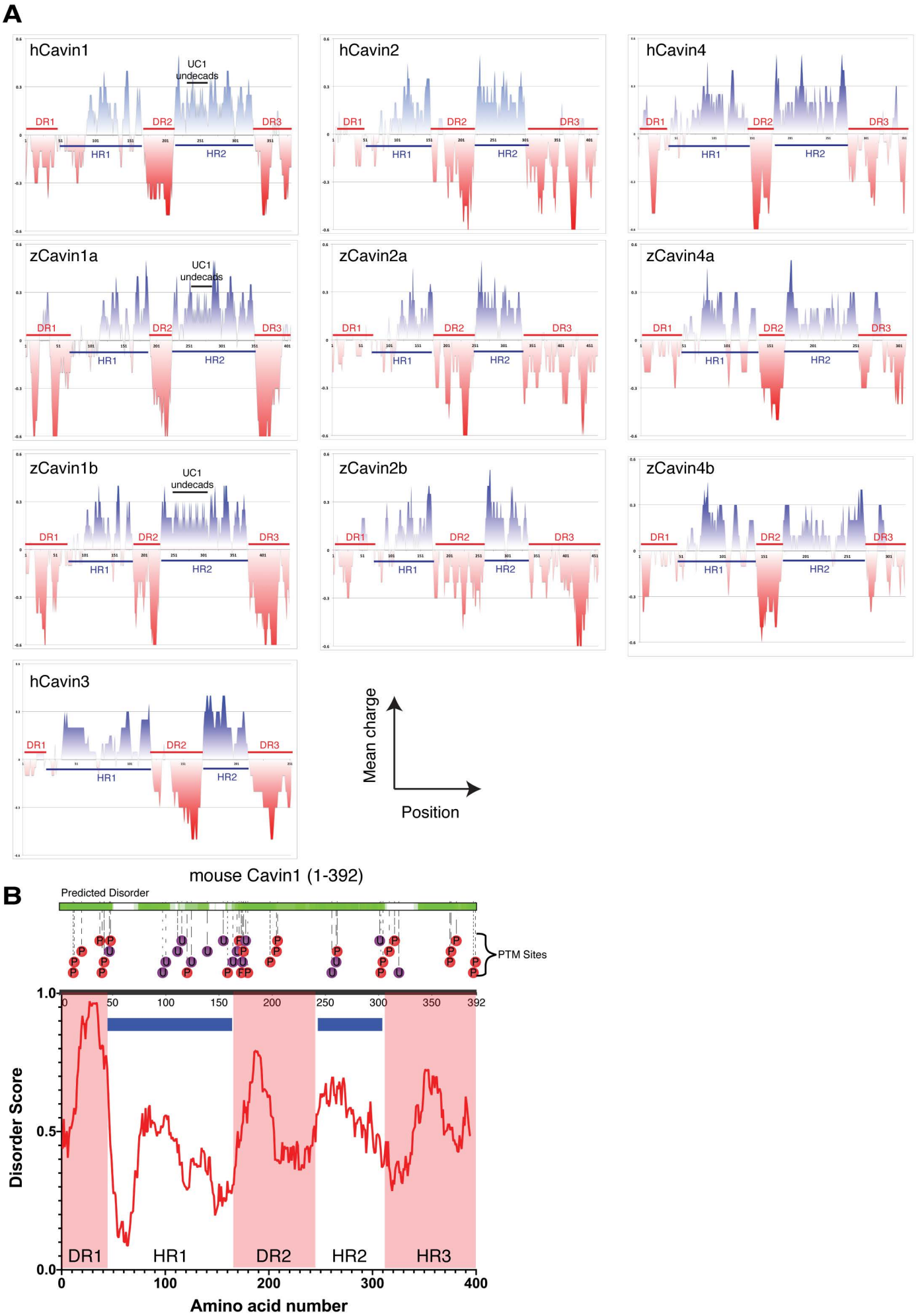

Figure S1. Electrostatic charge distribution and sequence disorder in the Cavin family proteins.
(A) Protein charge plots of human (h) and zebrafish (z) cavin family proteins performed using the Emboss Server (http://www.bioinformatics.nl/cgi-bin/emboss/charge) (using standard input parameters and a window width of five amino acid residues). (B) The Cavin1 sequence was analysed using the D2P2 web server 15 for predicted regions of disorder, and also known sites of post-translational modifications.

Mouse Cavin1 bacterial expression constructs

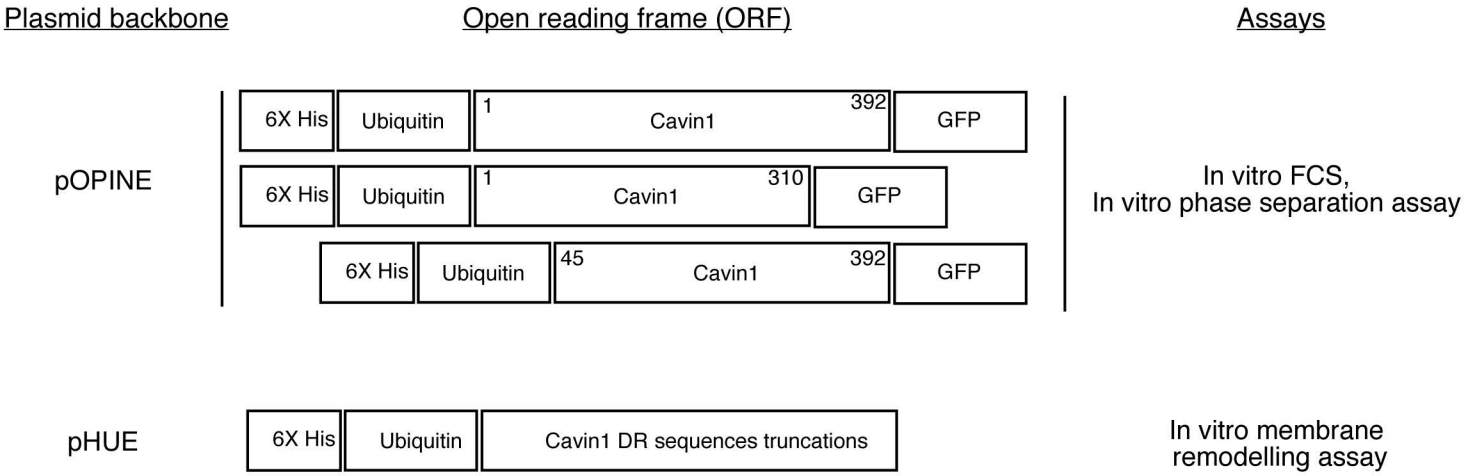

Dog CAV1 bacterial expression constructs

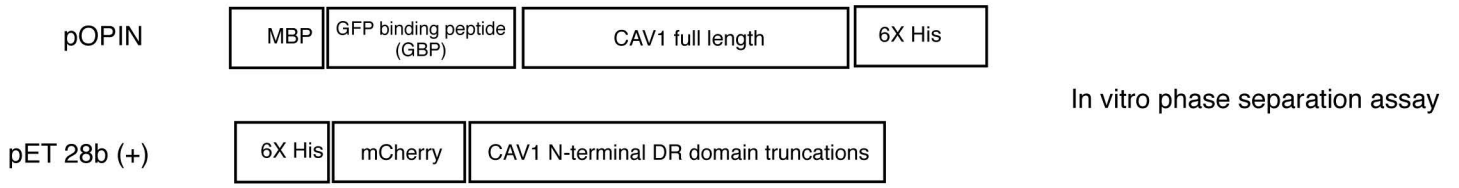

Mouse Cavin1 mammalian expression constructs

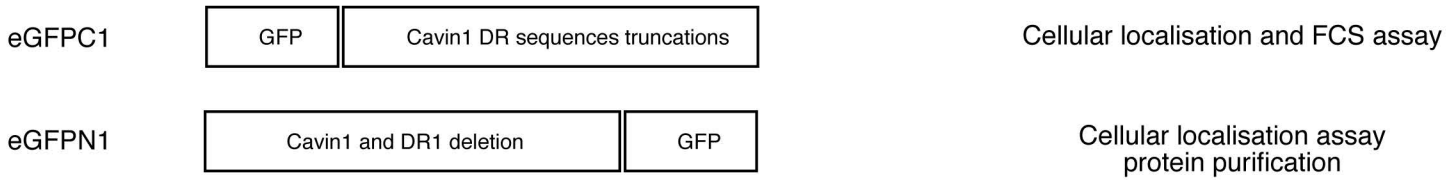

Figure S2. Schematic representation of protein expression constructs used in this study.

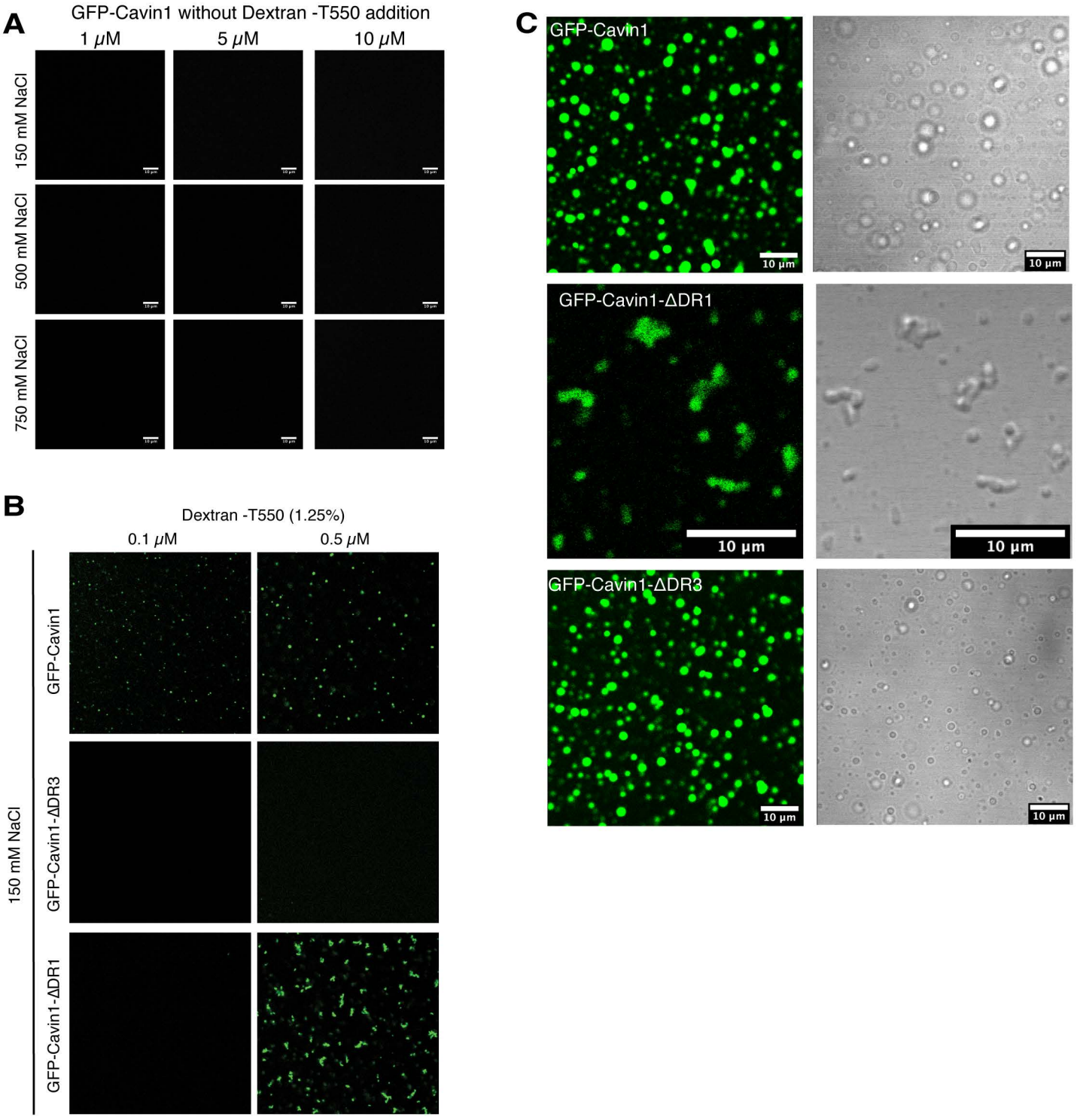

Figure S3. LLPS behaviour of recombinant Cavin1 expressed in bacteria
(A) Liquid-liquid phase separation (LLPS) assay with bacterially expressed recombinant Ub- and GFP-tagged Cavin1, at different protein and salt concentrations but in the absence of dextran or other crowding agents. (B) At low concentrations, full length Cavin1 still forms liquid droplets, and Cavin1-ΔDR1 still forms coacervates. Cavin1-ΔDR3 is less prone to LLPS at low concentrations compared to the full-length protein. (C) LLPS assay performed with GFP tagged Cavin1-ΔDR1 by addition of 1.25% dextran T-500. Fluorescent GFP signal and adjacent bright filed image showing transparent drops unlike non-specific precipitates that are usually non-transparent and milky or brown in appearance. Scale bar – 10 μm.

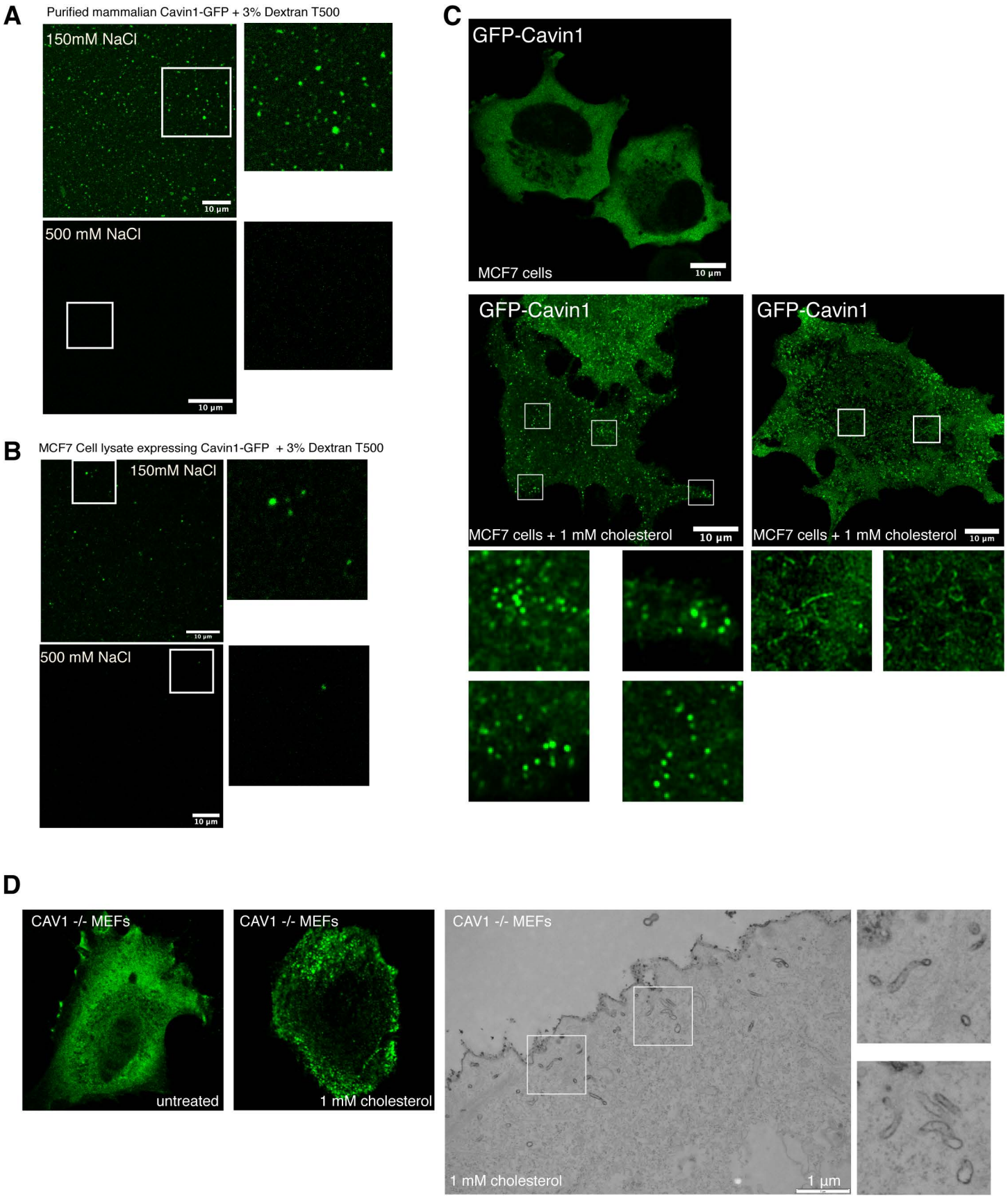

Figure S4. Cavin1 undergoes LLPS and remodels cellular membranes devoid of CAV1.
(A) LLPS assay performed with Cavin1-GFP expressed and purified from mammalian HEK293 cells. (B) MCF7 cell lysates expressing Cavin1-GFP with the addition of 3% dextran T-500 in either 150 mM NaCl or 500 mM NaCl. Scale bar – 10 μm. (C) MCF7 cells expressing GFP-Cavin1, Cavin1-ΔDR1 showing cytosolic distribution and Cavin1-ΔDR3 showing diffuse localisation (upper panel). Addition of a water-soluble form of cholesterol (1 mM added, with effective available cholesterol concentration ~40 μM) to cells expressing GFP-Cavin1 promotes liquid like droplet formation, membrane recruitment, and in some cells and tubulation in some cells (lower panels). Scale bar – 10 μm. (D) CAV1-/- MEF cells expressing GFP-Cavin1 show cytosolic distribution and addition of 1 mM cholesterol causes membrane recruitment of GFP-Cavin1 (left panels) also observed by ruthenium red labelling of membrane surface by EM. Scale bar – 1 μm.

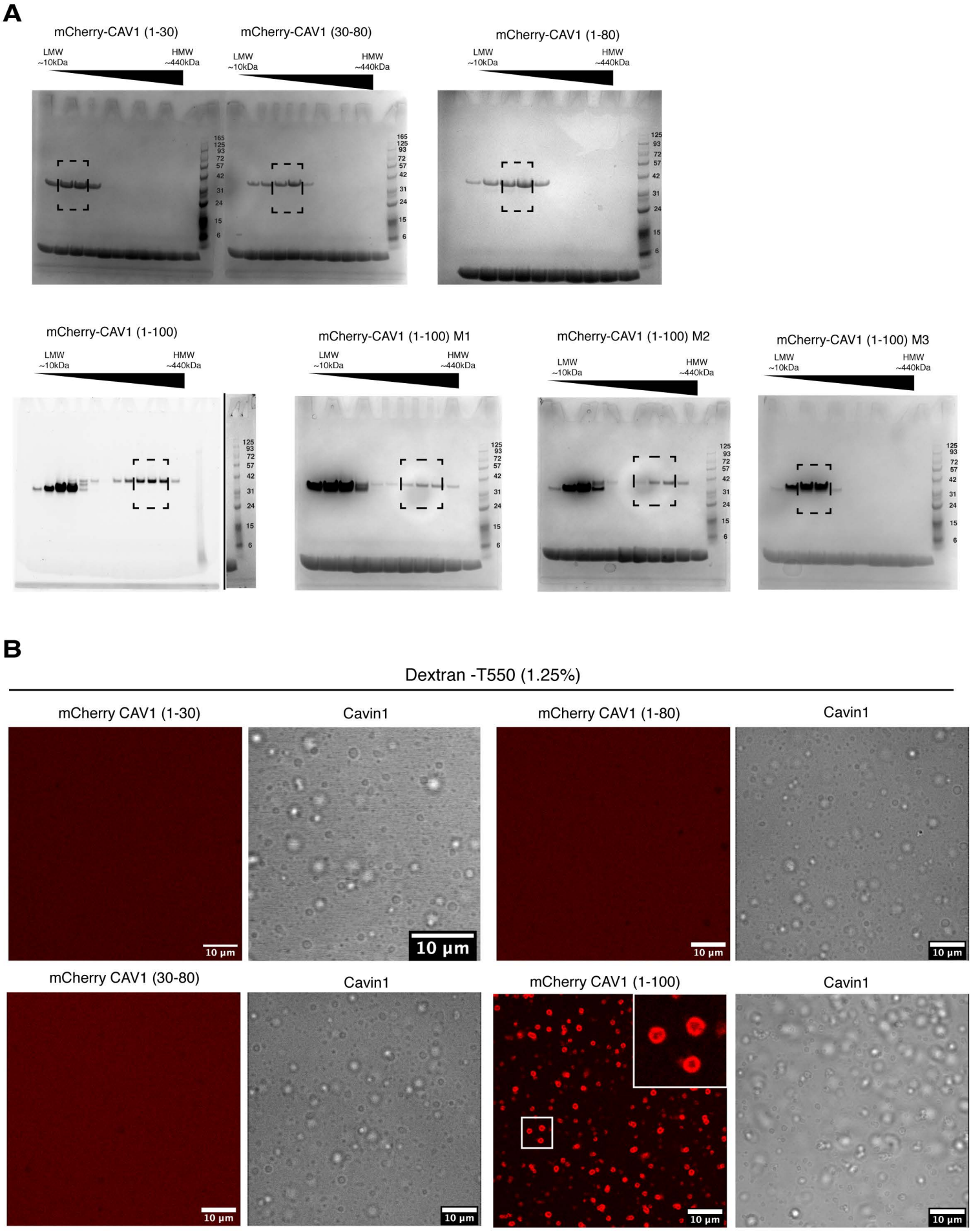

Figure S5. Co-phase separation of CAV1 with Cavin1.
(A) In gel fluorescence images of gel filtration fractions for respective mCherry-tagged CAV1 mutants. (B) LLPS assay with mCherry CAV1 (1-30), (30-80), (1-80) and (1-100) and Cavin1. mCherry-CAV1 (1-100) is recruited to cavin1 droplets and undergo LLPS.

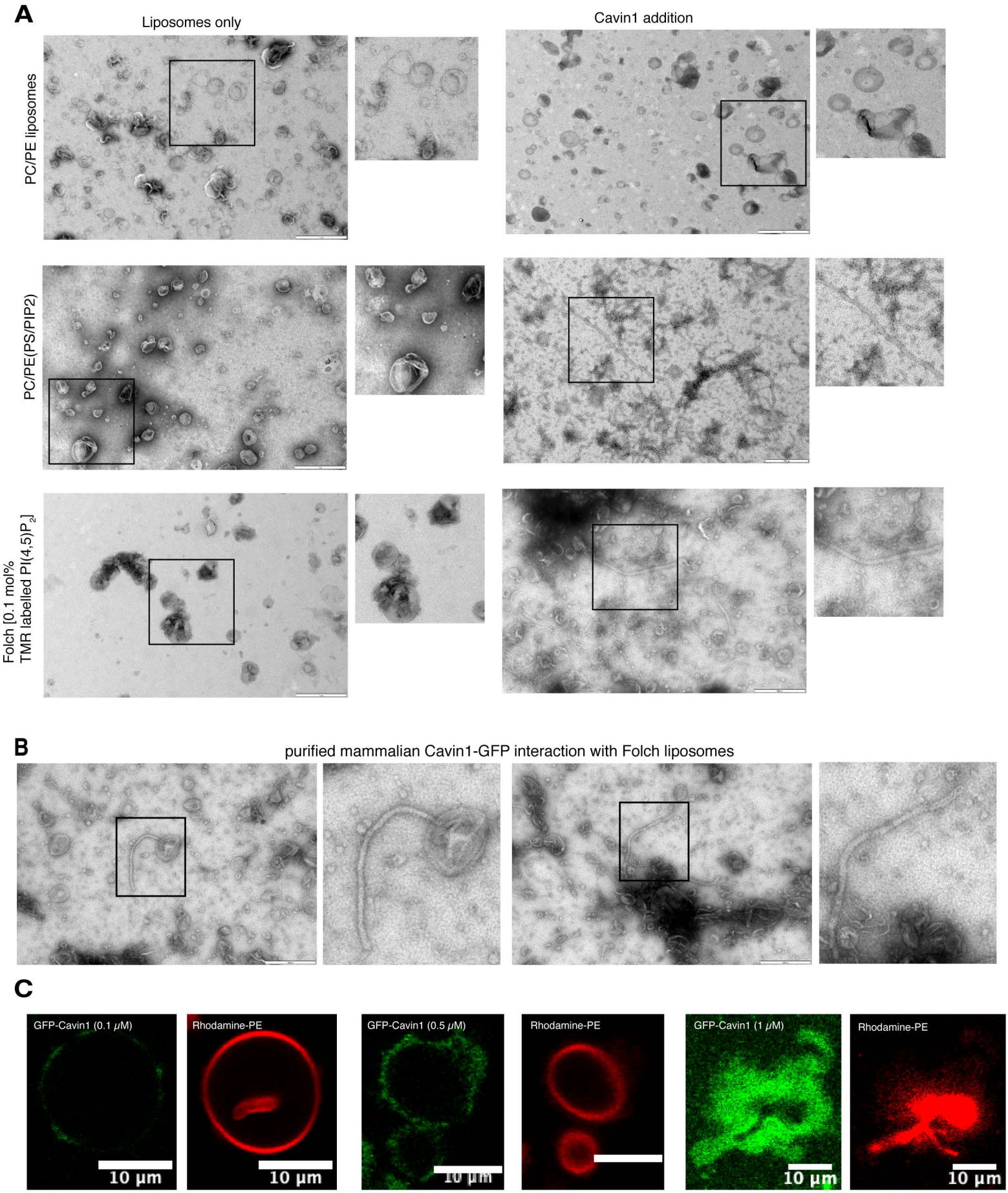

Figure S6. Cavin1 membrane interactions in vitro
(A) In vitro membrane tubulation assay and negative stain electron microscopy was performed after mixing Cavin1 and liposomes consisting of Phosphatidylcholine (PC) and Phosphatidylethanolamine (PE) or PC/PE liposomes containing PI(4,5)P2 and Phosphatidylserine (PS) or Folch liposomes containing 0.1 mol% TMR labelled PI(4,5)P2 to replicate conditions in Figure 5. (B) In vitro membrane tubulation assay performed by mixing mammalian Cavin1-GFP with Folch liposomes, with membrane tubules highlighted in insets. Scale bar – 1 μm. (C) Dose dependent GFP-Cavin1 interaction with GUVs containing rhodamine-PE or Bodipy-TMR-PI(4,5)P2.

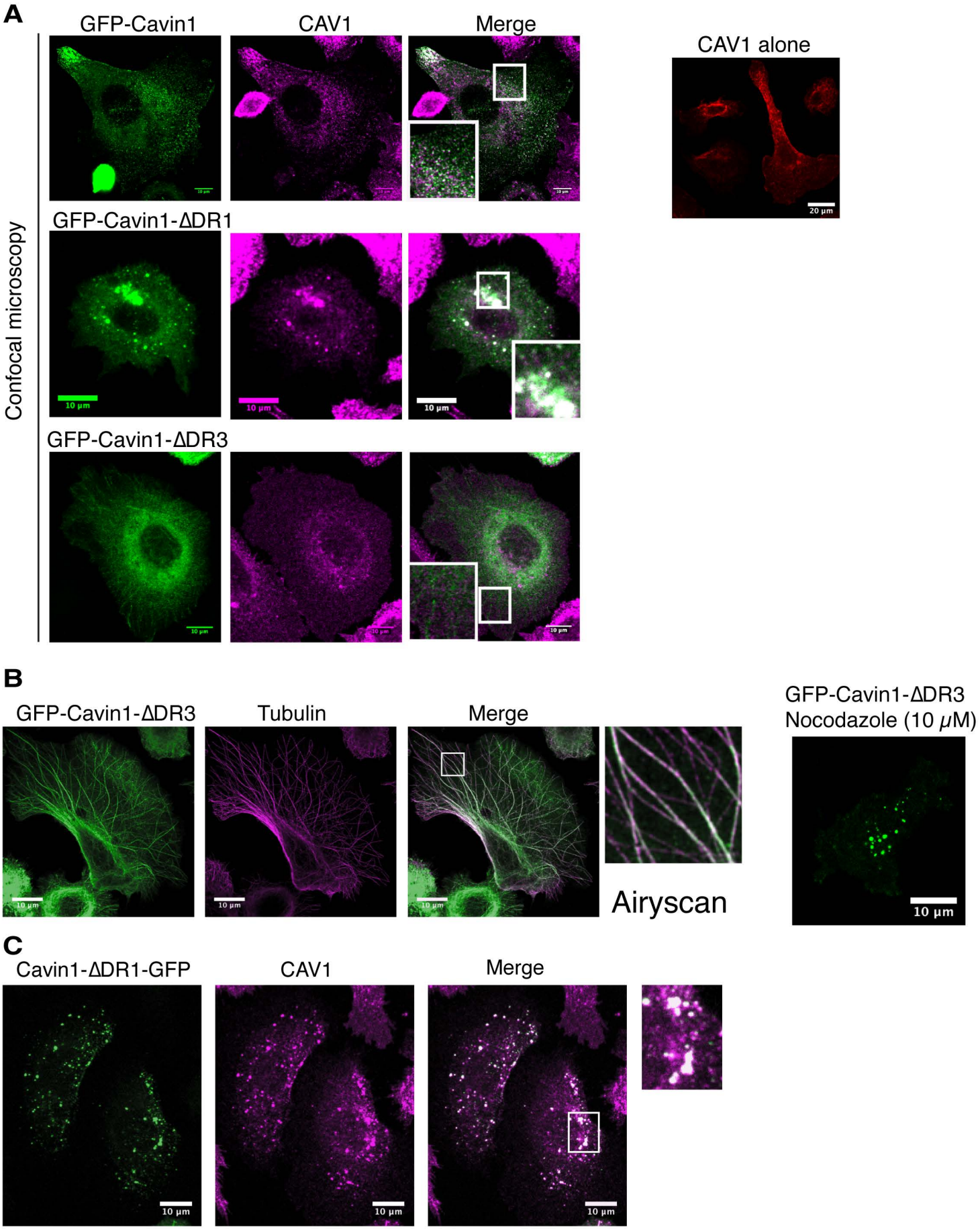

Figure S7. Localisation of Cavin1 with truncated DR1 and DR3 domains.
(A) Confocal microscopy images of GFP-Cavin1, GFP-Cavin1-ΔDR1 and GFP-Cavin1-ΔDR3 immunolabelled with CAV1 (red) (B) GFP-Cavin1-ΔDR3 (green) associates with microtubules (red) in PC3 cells and disperses to the cytosol and forms liquid droplets after nocodazole treatment. Fluorescence images acquired with a Zeiss Airyscan2 microscope. (C) Cavin1-ΔDR1-GFP with a C-terminal GFP tag shows a similar intracellular accumulation with CAV1 in PC3 cells as the N-terminal GFP-tagged protein (Fig. 6A), suggesting that the GFP tag does not contribute to this phenotype.

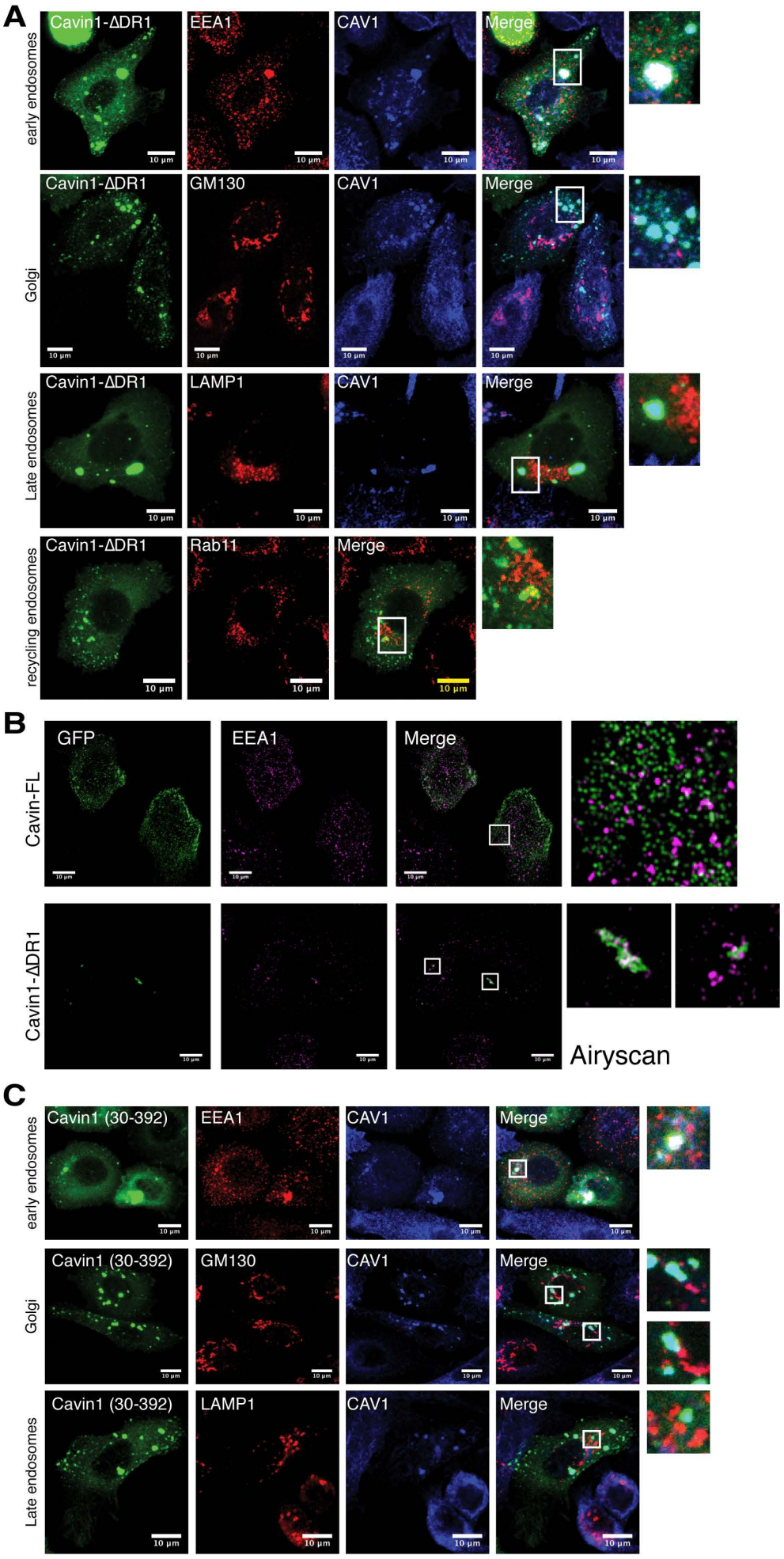

Figure S8. Comparison of Cavin1 truncation mutants with endocytic markers.
(A) GFP-tagged Cavin1-ΔDR1 (green) was expressed in PC3 cells, and fixed cells were immunolabelled for CAV1 (blue) and different endocytic markers (red) including EEA1, GM130, LAMP1 and Rab11. Only EEA1 showed significant overlap with the internalised Cavin1-ΔDR1 and CAV1 positive structures. (B) High-resolution images of GFP-tagged Cavin1 and Cavin1-ΔDR1 (green) in PC3 cells compared with EEA1 (magenta) acquired with a Zeiss Airyscan2 microscope. (C) As for (A) but cells expressing GFP-tagged Cavin1(30-392). Cavin1(30-392) accumulates at intracellular structures with CAV1 and positive for EEA1 labelling similarly to Cavin1-ΔDR1 with the full deletion of the DR1 domain.

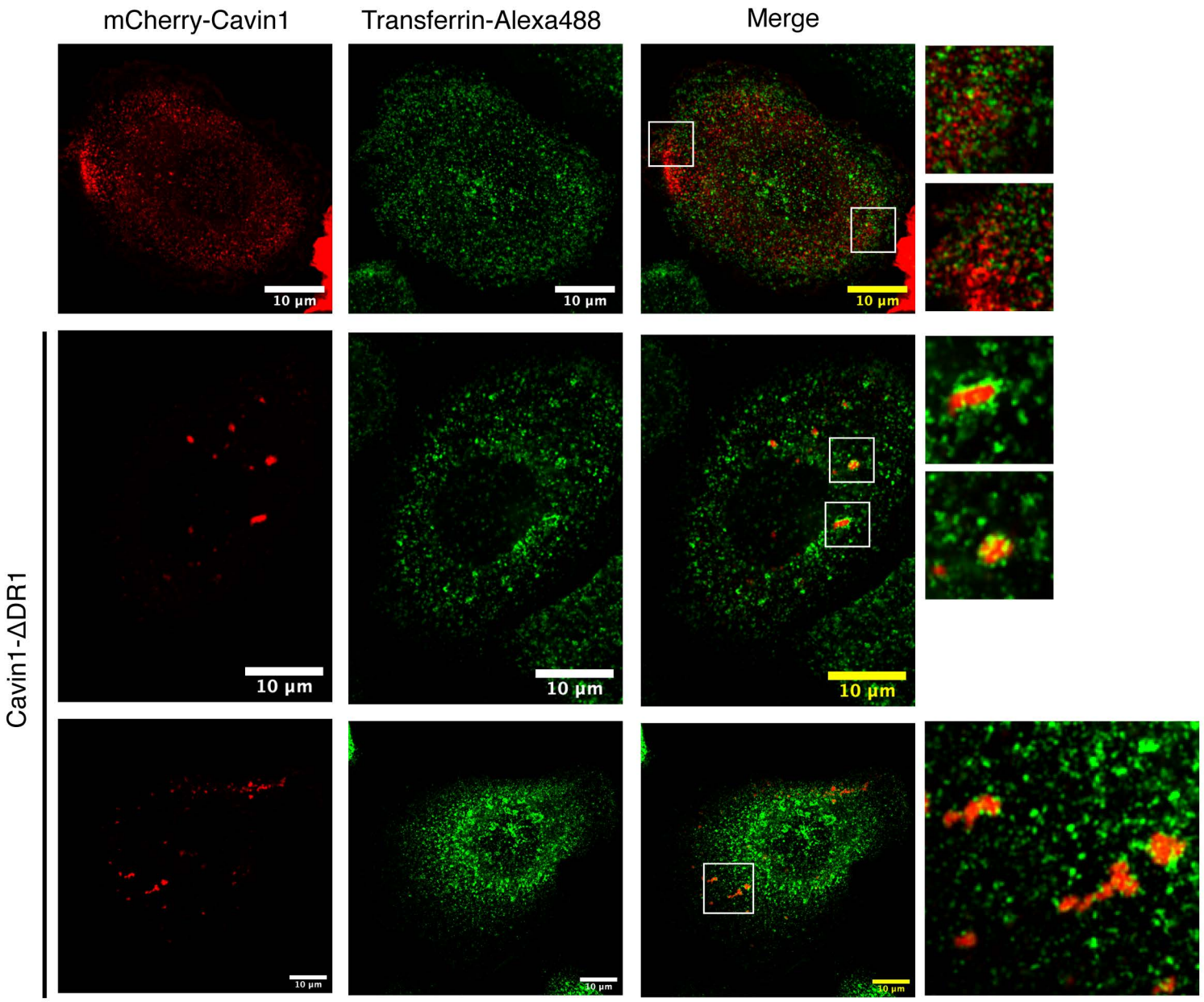

Figure S9. Cavin1-ΔDR1 shows colocalisation with internalised transferrin.
Transferrin uptake assay was performed in PC3 cells expressing either mCherry-tagged Cavin1 or Cavin1-ΔDR1 (red) with transferrin Alexa-488 (green). Wild-type mCherry-Cavin1 showed no colocalization with endocytosed transferrin whereas mCherry-Cavin1-ΔDR1 formed large structures (red) with transferrin positive endosomes surrounding them.

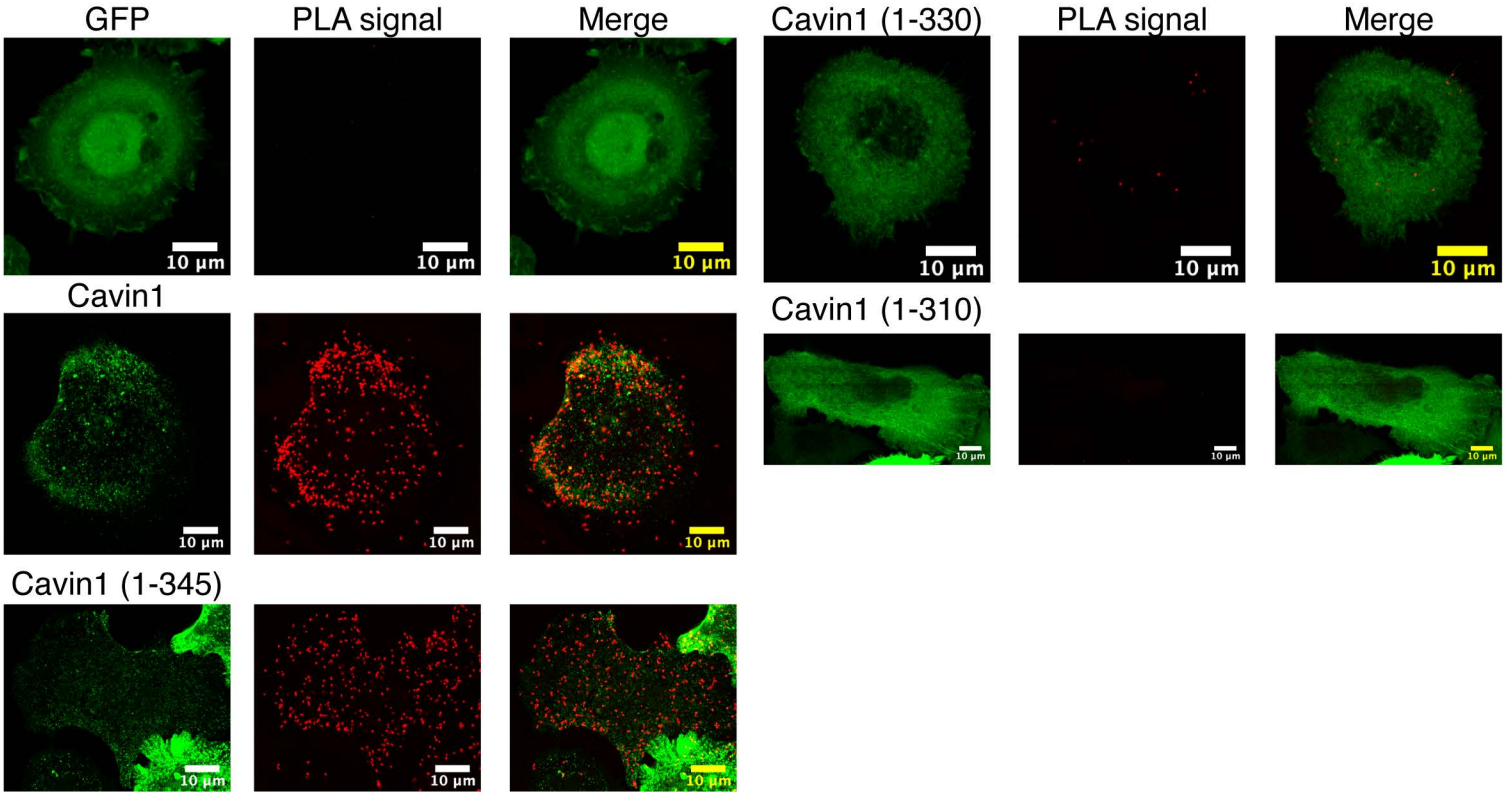

Figure S10. PLA assay of Cavin1 interactions with CAV1
Representative images of proximity ligation assays of Cavin1 and CAV1 interactions, with GFP-tagged Cavin1 mutants in green and PLA signal in red . Scale bar – 10 µm. Related to Fig. 7C.

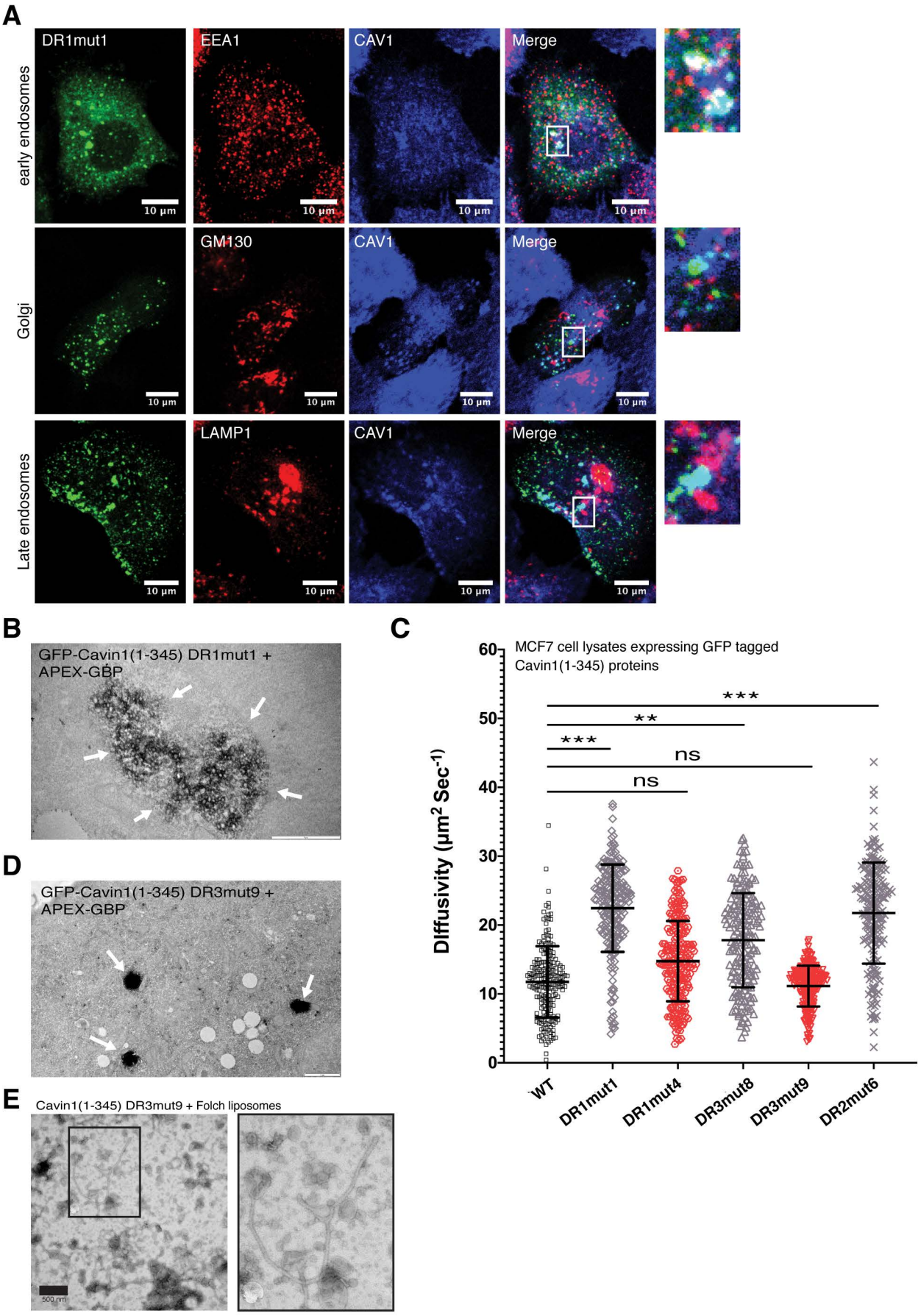

Figure S11. Localisation and membrane remodelling by Cavin1(1-345) mutant proteins.
(A) GFP-tagged Cavin1(1-345) mutant M1 was expressed in PC3 cells, and fixed cells were immunolabelled for CAV1 (blue) and different endocytic markers (red) including EEA1, GM130, and LAMP1. Like the complete deletion of the residues 1-30 in the Cavin1 DR1 region (Fig. S7C) Cavin1(1-345) mutant M1 shows significant overlap with CAV1 and EEA1 positive internal structures. (B) APEX-GBP labelling of GFP-tagged Cavin1(1-345) mutant M1 shows accumulation and clustering with internal membrane vesicles (arrows). (C) The diffusion rate measured by FCS of selected GFP-tagged Cavin1(1-345) DR mutants in lysates after expression in MCF7 cells (lacking endogenous Cavins and Caveolins). N = 3, n = 15-25. Error bars indicate mean ± SD, **P<0.05, *** P<0.001, ns – not significant. (D) APEX-GBP labelling of GFP-tagged Cavin1(1-345) mutant M4 shows droplet localisation (arrows). (E) Purified Ub-tagged Cavin1(1-345) mutant M4 was mixed with unilamellar Folch liposomes (extruded to 400 nm diameter) and analysed by negative stain EM (1% uranyl acetate). This mutant is able to remodel and tubulate these synthetic membranes, although with a slightly larger diameter than wild-type Cavin or Cavin1(1-345) (Fig. 4D).

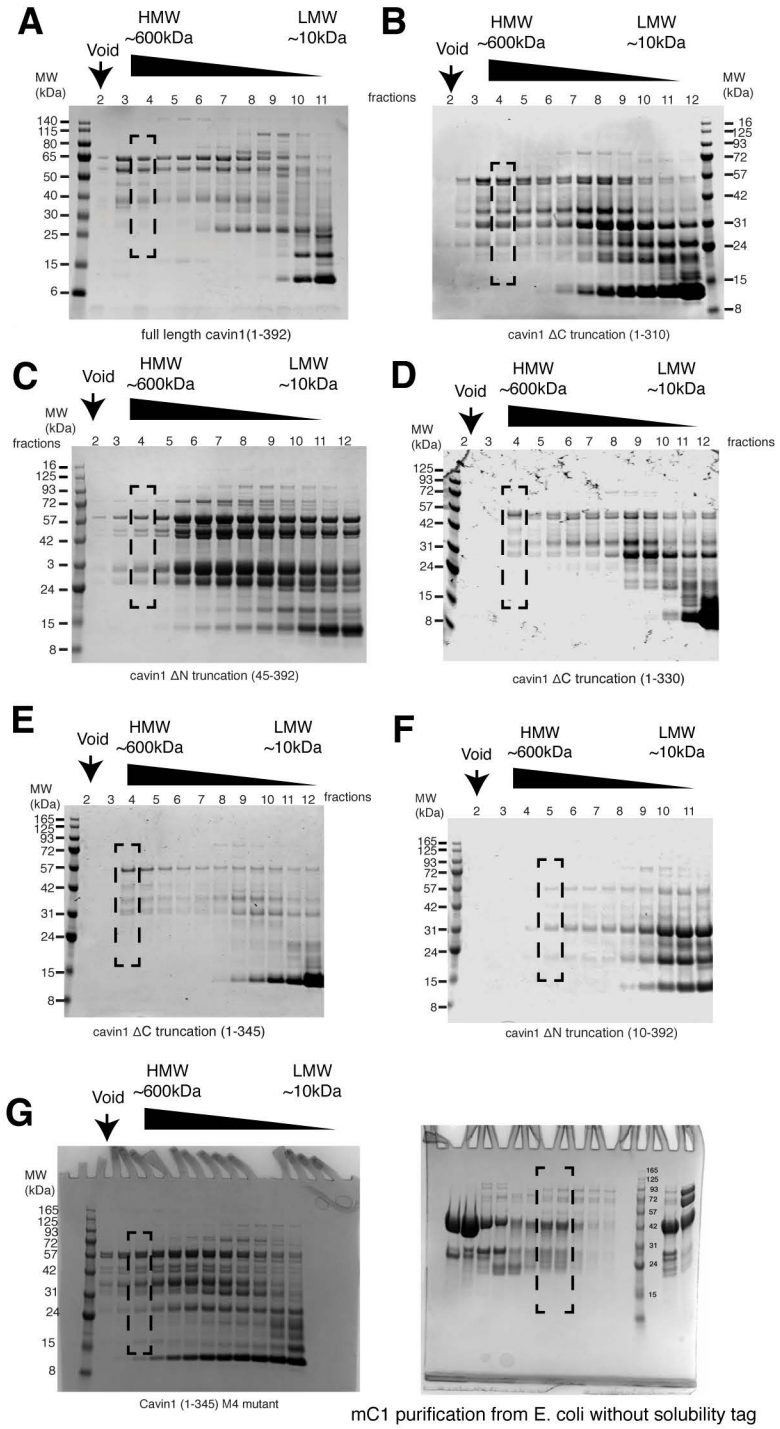

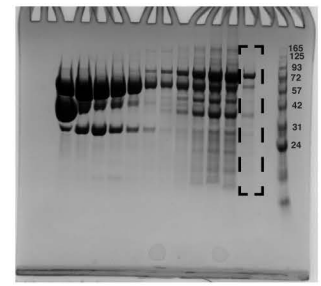

MBP-(GBP:GFP)-CAV1 purification

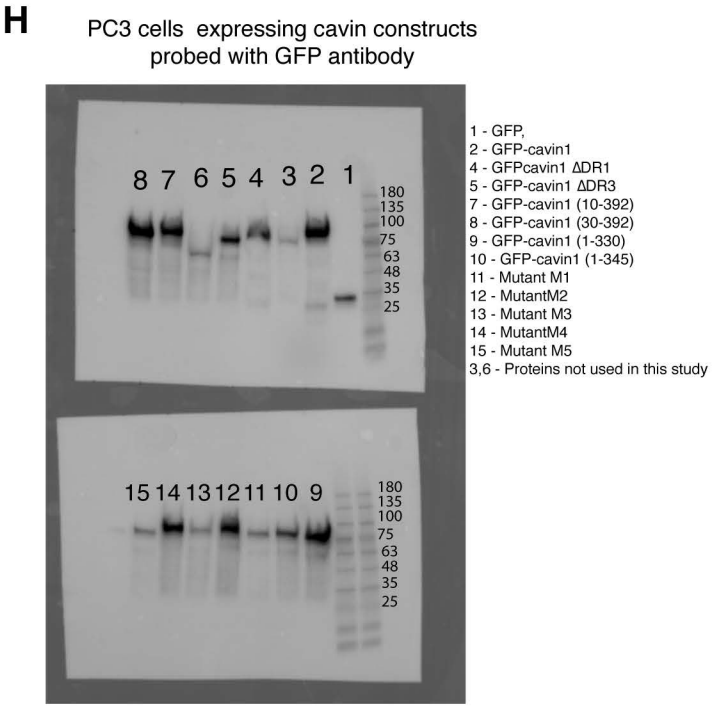

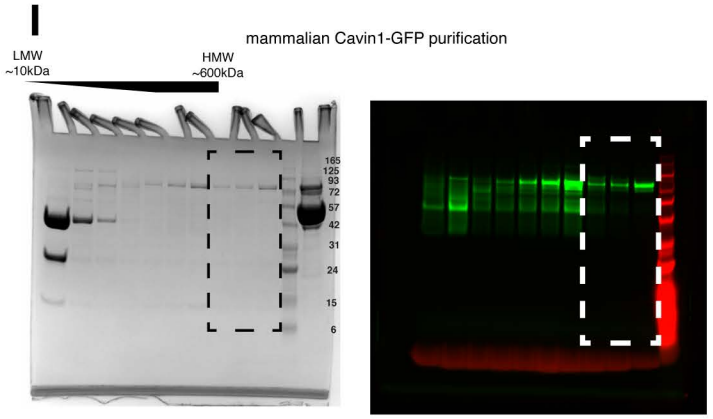

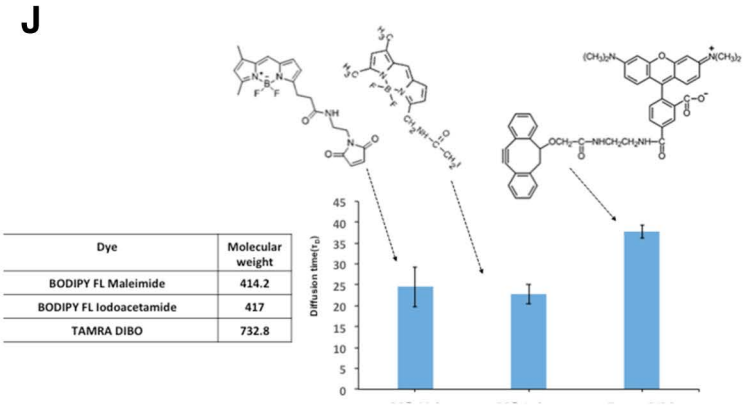

Dye	Molecular weight
BODIPY FL Maleimide	414.2
BODIPY FL Iodoacetamide	417
TAMRA DIBO	732.8

Figure S12. Gels showing bacterially expressed purified recombinant Cavin1 proteins used in this study (A to G). (H) and Western blot showing expression of GFP tagged mutants expressed in PC3 cell line probed with anti-GFP antibody. (I) SDS-PAGE and in gel fluorescence profile of Cavin1-GFP purified from HEK cells using GFP nanobody and subjected size exclusion chromatography on superose 6 (10/300) column. (J) The diffusion time measurements for three dyes performed before each FCS session.